Vlasov–Maxwell equations with spin effects

**Nicolas Crouseilles[1],[†], Paul-Antoine Hervieux[2], Xue Hong[1] and
Giovanni Manfredi [2],[†]**

[1]Univ Rennes and Inria centre de l'université de Rennes and IRMAR UMR 6625, 35042 Rennes, France

[2]Université de Strasbourg, CNRS, Institut de Physique et Chimie des Matériaux de Strasbourg, UMR 7504, F-67000 Strasbourg, France

We present a numerical method to solve the Vlasov–Maxwell equations for spin-1/2 particles, in a semiclassical approximation where the orbital motion is treated classically while the spin variable is fully quantum. Unlike the spinless case, the phase-space distribution function is a 2×2 matrix, which can also be represented, in the Pauli basis, as one scalar function f_0 and one three-component vector function $\boldsymbol{f}$. The relationship between this 'vectorial' representation and the fully scalar representation on an extended phase space first proposed by Brodin *et al.* (*Phys. Rev. Lett.*, vol. 101, 2008, p. 245002) is analysed in detail. By means of suitable approximations and symmetries, the vectorial spin-Vlasov–Maxwell model can be reduced to two-dimensions in the phase space, which is amenable to numerical solutions using a high-order grid-based Eulerian method. The vectorial model enjoys a Poisson structure that paves the way to accurate Hamiltonian split-time integrators. As an example, we study the stimulated Raman scattering of an electromagnetic wave interacting with an underdense plasma, and compare the results with those obtained earlier with the scalar spin-Vlasov–Maxwell model and a particle-in-cell code.

Key words: plasma simulation, quantum plasma, plasma dynamics

1. Introduction

To study the interaction between electromagnetic fields and metallic (nano-)objects, it is possible, as a first approximation, to model the conduction electrons as a free electron plasma confined by the attractive Coulomb forces of the nuclei. However, the electrons carry, besides an electric charge, also a half-integer spin, which can play a significant role in their dynamics, most notably for intense and ultrashort laser pulses. Spin effects play an important role through the Zeeman effect, the spin-orbit interaction (Hinschberger & Hervieux 2012; Krieger *et al.* 2015, 2017) and spin currents (Choi *et al.* 2014; Schellekens *et al.* 2014; Hurst, Hervieux & Manfredi 2018), and they are involved in the complex mechanisms leading to the loss of magnetization on a femtosecond time scale (Beaurepaire *et al.* 1996; Bigot, Vomir & Beaurepaire 2009; Bigot & Vomir 2013).

† Email addresses for correspondence: nicolas.crouseilles@inria.fr,
giovanni.manfredi@ipcms.unistra.fr

Spin effects are usually described using standard approaches, such as the Hartree–Fock equations and the time-dependent density functional theory (Krieger *et al.* 2015), or, more recently, quantum hydrodynamic models (Moldabekov, Bonitz & Ramazanov 2018). In recent years, phase-space approaches issued from plasma physics research have been introduced as an alternative to the above models. These models make use of kinetic equations similar to the standard Vlasov equation, which describes the evolution of a probability distribution in the relevant phase space, and can be broadly grouped into two families: (i) models that use a scalar distribution function defined on an extended phase space (x, p, s), where x denotes the position, p the momentum and s the spin variable on the unit sphere (Brodin *et al.* 2008, 2011; Marklund, Zamanian & Brodin 2010; Zamanian, Marklund & Brodin 2010); (ii) models for which the distribution function is a 2×2 matrix that evolves in the standard classical phase space (x, p) (Hurst *et al.* 2014; Manfredi, Hervieux & Hurst 2019); this 2×2 distribution function can also be represented, in the so-called Pauli basis, as one scalar function f_0 and one three-component vector function f, for which reason we shall term these models 'vectorial'. For both approaches, one assumes that the orbital motion is classical (hence the use of a standard Vlasov-like probability distribution), while the spin is treated as a fully quantum variable.

The relationship between the two types of models was not hitherto perfectly clear, in particular under what assumptions they are exactly equivalent. The first part of the present work will be devoted to clarify this important issue. Indeed, the vectorial distribution functions can be seen as the zeroth- and first-order 'moments' (in spin space) of the scalar distribution function $f(x, p, s)$, and the vectorial equations as the evolution equations for such moments. This is the same relationship that exists between the Vlasov distribution function and its velocity moments, which obey a set of fluid equations. In the Vlasov/fluid analogy, the velocity moment equations are not equivalent to the full kinetic model, except if one prescribes a closure relation and this relation is preserved by the evolution of the kinetic equation.[1] In our spin case, the closure relation implies that the scalar distribution function $f(x, p, s)$ should be a linear function of s (Zamanian *et al.* 2010; Manfredi *et al.* 2019). When this relation is satisfied for all times, taking the zeroth- and first-order moments of the scalar distribution leads to the evolution equations of the vectorial model and guarantees the equivalence between the two approaches. This important point will be discussed in detail in this work, in particular the role played by the quantum magnetic dipole term in the scalar model (which contains derivatives in both real and spin space, thus making particle-in-cell (PIC) methods much more involved).

From a numerical point of view, the two approaches are intrinsically different, and have their own advantages and drawbacks with respect to the available numerical techniques. Indeed, due to the high dimensionality of the extended phase space (three dimensions for position, three for momentum, and two for the spin), the scalar model is not adapted to grid-based (Eulerian) numerical methods. Instead, they are naturally adapted for PIC methods (Crouseilles *et al.* 2021), for which the extra number of dimensions is not an obstacle as it only represents two more (spin) labels for the trajectories. In contrast, the vectorial approach is more easily amenable to Eulerian solvers, since it merely implies the solution of four Vlasov equations instead of one for spinless particles. Moreover, the presence of the quantum magnetic dipole term (involving cross-derivatives in both p and s) makes the scalar model quite awkward to solve numerically, whereas the corresponding term in the vector model does not raise any particular difficulty. For this reason, in our

---

[1]Such exact closure relations are known to exist. For instance, the Vlasov evolution of a 'water-bag' distribution function (constant within a closed phase-space contour and zero outside) is exactly equivalent to a set of fluid equations.

earlier work using a PIC code (Crouseilles *et al.* 2021) this additional term was not taken into account.

We note that other PIC approaches (Brodin, Holkundkar & Marklund 2013) did not employ the extended phase space mentioned above, but considered two separate spin-up and spin-down populations for the electrons. Similarly, Tonge, Dauger & Decyk (2004) and Dauger, Decyk & Dawson (2005) have extended classical PIC methods to the quantum regime (without spin) using an approach based on Feynman path integrals. Very recently, PIC simulation methods for particles with spin were developed and validated by (Li *et al.* 2021) for applications to laser–plasma interactions.

In the present work, we propose an Eulerian method to solve numerically the self-consistent vectorial spin-Vlasov–Maxwell equations in the broad context of laser–plasma interactions. As the full six-dimensional phase space is still very demanding for Eulerian methods in terms of computational costs, we have considered a simpler one-dimensional (1-D) problem (two-dimensional phase space) obtained by assuming that the electrons are cold in the transverse plane with respect to the direction of propagation of the incident electromagnetic field. This model is thus described by the distribution functions $(f_0, \boldsymbol{f})(t, x, p) \in \mathbb{R}^4$, with $t \geq 0$ and $(x, p) \in \mathbb{R}^2$.

The vectorial model enjoys a Poisson structure which paves the way to a suitable time splitting integrator. Following the recent development of geometric numerical method for Vlasov-type equations (Crouseilles, Einkemmer & Faou 2015; Li, Sun & Crouseilles 2020; Crestetto *et al.* 2022), we first discretize in time by using a Hamiltonian splitting, which leads to different subsystems to solve. It turns out that the Hamiltonian splitting leads to very simple subsystems that can be solved exactly in time, and for which grid-based methods (Fourier in space and finite volume in momentum) can be used to obtain a very accurate solver.

In our earlier work (Crouseilles *et al.* 2021), we dealt with the same laser–plasma problem, but used the scalar approach and a PIC numerical method. Even though PIC methods are known to give good results for a moderate number of particles, the convergence rate is slow, as it depends on the square root of the number of particles. By studying the influence of several physical parameters (temperature, electromagnetic field amplitude, quantum effects, etc.) on the Raman instability, we observed that an initially polarized electron gas can lose its polarization through a combination of thermal effects and the Raman instability.

Here, we perform the same study solving the vectorial spin-Vlasov–Maxwell equations with a Eulerian numerical method. Even though the two models are not mathematically equivalent (because in the PIC approach we neglected the quantum magnetic dipole term involving cross-derivatives in $\boldsymbol{p}$ and $\boldsymbol{s}$), it is interesting to compare the results for various values of the physical parameters, such as the temperature and the effective Planck constant. Indeed, the two models (scalar and vector) become equivalent in the classical limit, although some differences can of course still arise because of the different numerical methods used to solve the evolution equations.

All in all, the present work should provide some useful guidelines on the choice of suitable numerical methods to simulate the semiclassical dynamics of a spin-polarized electron gas.

2. Spin-Vlasov–Maxwell models

In this section, we recall the governing equations for the scalar spin Vlasov–Maxwell system in the extended phase space $(\boldsymbol{x}, \boldsymbol{p}, \boldsymbol{s})$ (see Marklund *et al.* 2010; Zamanian *et al.* 2010; Marklund & Morrison 2011; Manfredi *et al.* 2019) and the corresponding vector system in the standard phase space $(\boldsymbol{x}, \boldsymbol{p})$ (see Hurst *et al.* 2014, 2017; Manfredi, Hervieux

& Crouseilles 2022). Both models are semiclassical approximations, in the sense that the orbital motion is treated with classical trajectories, whereas the spin degrees of freedom are fully quantum. We shall discuss the equivalence between the two models and clarify the role of the different terms in the equations. The general case (three dimensions in space and momentum) will be considered first, after which we will focus on the reduced model used for the forthcoming laser plasma application (one dimension in space and momentum).

The models will be presented in a dimensionless form, where time is normalized to the inverse of the plasma frequency $\omega_p = \sqrt{n_0 e^2 / m \epsilon_0}$, velocities are normalized to c, and length to c/ω_p. Here, e denotes the electron charge, c the speed of light, $\hbar$ the reduced Planck constant, m the electron mass, ϵ_0 the permittivity of vacuum and n_0 the fixed ion density. In these units, electric fields are normalized to $mc\omega_p/e$, and the scaled Planck constant is $\mathfrak{h} = \hbar\omega_p/2mc^2$.

2.1. *Scalar and vector models in three dimensions*

2.1.1. *Scalar model*

The scalar model, which was put forward in several earlier works (Marklund *et al.* 2010; Zamanian *et al.* 2010; Marklund & Morrison 2011; Manfredi *et al.* 2019), is described by a scalar electron distribution function that depends on the extended phase space variable plus time,

$$f : (t, \boldsymbol{x}, \boldsymbol{p}, \boldsymbol{s}) \in \mathbb{R}_+ \times \mathbb{R}^3 \times \mathbb{R}^3 \times \mathbb{R}^3 \mapsto f(t, \boldsymbol{x}, \boldsymbol{p}, \boldsymbol{s}) \in \mathbb{R}, \qquad (2.1)$$

together with the self-consistent electromagnetic fields $(\boldsymbol{E}, \boldsymbol{B}) : (t, \boldsymbol{x}) \mapsto (\boldsymbol{E}, \boldsymbol{B})(t, \boldsymbol{x}) \in \mathbb{R}^3 \times \mathbb{R}^3$. These quantities obey the following Vlasov–Maxwell system (Crouseilles *et al.* 2021):

$$
\begin{cases}
\dfrac{\partial f}{\partial t} + \boldsymbol{p} \cdot \nabla f + \left[\boldsymbol{E} + \boldsymbol{p} \times \boldsymbol{B} + \beta\mathfrak{h}\nabla(\boldsymbol{s} \cdot \boldsymbol{B}) + \gamma\mathfrak{h}\nabla\left(\boldsymbol{B} \cdot \dfrac{\partial}{\partial \boldsymbol{s}}\right) \right] \cdot \dfrac{\partial f}{\partial \boldsymbol{p}} + \boldsymbol{s} \times \boldsymbol{B} \cdot \dfrac{\partial f}{\partial \boldsymbol{s}} = 0, \\[2ex]
\dfrac{\partial \boldsymbol{E}}{\partial t} = \nabla \times \boldsymbol{B} - \displaystyle\int_{\mathbb{R}^6} \boldsymbol{p} f \, \mathrm{d}\boldsymbol{p} \, \mathrm{d}\boldsymbol{s} - \alpha\mathfrak{h}\nabla \times \int_{\mathbb{R}^6} \boldsymbol{s} f \, \mathrm{d}\boldsymbol{p} \, \mathrm{d}\boldsymbol{s}, \\[2ex]
\dfrac{\partial \boldsymbol{B}}{\partial t} = -\nabla \times \boldsymbol{E}, \\[2ex]
\nabla \cdot \boldsymbol{E} = \rho - 1, \quad \rho = \displaystyle\int_{\mathbb{R}^6} f \, \mathrm{d}\boldsymbol{p} \, \mathrm{d}\boldsymbol{s}, \quad \nabla \cdot \boldsymbol{B} = 0,
\end{cases}
\tag{2.2}
$$

with initial conditions

$$f(t = 0) = f^0, \quad \nabla \cdot \boldsymbol{E}^0 = \int_{\mathbb{R}^6} f^0 \, \mathrm{d}\boldsymbol{p} \, \mathrm{d}\boldsymbol{s} - 1, \quad \boldsymbol{B}(t = 0) = \boldsymbol{B}^0 \text{ such that } \nabla \cdot \boldsymbol{B}^0 = 0,$$
$$\tag{2.2a–c}$$

where we have introduced the artificial parameters α, β, γ in order to facilitate the comparison with the vectorial model. Our earlier work (Crouseilles *et al.* 2021) used the above equations with $\alpha = 1$, $\beta = 1$ and $\gamma = 0$ (i.e. no cross-derivative in $\boldsymbol{s}$ and $\boldsymbol{p}$).

2.1.2. *Vector model*

The vectorial model follows the standard representation of quantum mechanics in terms of density matrices, which are 2×2 matrices for spin-1/2 fermions. The corresponding

Wigner function is also a 2×2 matrix $W(t, \boldsymbol{x}, \boldsymbol{p}) \in \mathcal{M}_{2,2}(\mathbb{C})$. The scalar distribution function is related to this matrix Wigner function by the formula (Manfredi *et al.* 2019)

$$
\begin{aligned}
f(t, \boldsymbol{x}, \boldsymbol{p}, \boldsymbol{s}) &= \frac{1}{2\pi} \sum_{j,k=1}^{2} \frac{1}{2} [\delta_{j,k} + \boldsymbol{s} \cdot \boldsymbol{\sigma}_{j,k}] W_{k,j}(t, \boldsymbol{x}, \boldsymbol{p}) \\
&= \frac{1}{4\pi}(1 + s_3) W_{1,1}(t, \boldsymbol{x}, \boldsymbol{p}) + \frac{1}{4\pi}(s_1 - is_2) W_{2,1}(t, \boldsymbol{x}, \boldsymbol{p}) \\
&\quad + \frac{1}{4\pi}(s_1 + is_2) W_{1,2}(t, \boldsymbol{x}, \boldsymbol{p}) + \frac{1}{4\pi}(1 - s_3) W_{2,2}(t, \boldsymbol{x}, \boldsymbol{p}), \quad (2.3)
\end{aligned}
$$

where $\boldsymbol{\sigma} = (\sigma_x, \sigma_y, \sigma_z)$ denote the Pauli matrices, $\boldsymbol{s} = (s_1, s_2, s_3) \in \mathbb{S}^2$ ($\mathbb{S}^2$ being the sphere in $\mathbb{R}^3$), and $W_{\beta, \alpha}$ are the components of the Wigner function matrix (Zamanian *et al.* 2010). Note that the scalar distribution is a linear function of the spin variable $\boldsymbol{s}$. Hence, one can write

$$
\begin{pmatrix} W_{1,1}(t, \boldsymbol{x}, \boldsymbol{p}) & W_{1,2}(t, \boldsymbol{x}, \boldsymbol{p}) \\ W_{2,1}(t, \boldsymbol{x}, \boldsymbol{p}) & W_{2,2}(t, \boldsymbol{x}, \boldsymbol{p}) \end{pmatrix} = \int_{\mathbb{S}^2} f(t, \boldsymbol{x}, \boldsymbol{p}, \boldsymbol{s}) \frac{1}{2} \begin{pmatrix} 1 + 3s_3 & 3(s_1 - is_2) \\ 3(s_1 + is_2) & 1 - 3s_3 \end{pmatrix} d\boldsymbol{s}. \quad (2.4)
$$

Transforming to spherical coordinates on $\mathbb{S}^2$, $s_1 = \sin\theta \cos\varphi$, $s_2 = \sin\theta \sin\varphi$, $s_3 = \cos\theta$ with $\theta \in [0, \pi]$, $\varphi \in [0, 2\pi]$, we have

$$
\int_{\mathbb{S}^2} s_i \, d\boldsymbol{s} = 0, \quad \int_{\mathbb{S}^2} s_i s_j \, d\boldsymbol{s} = \delta_{i,j} \frac{4\pi}{3}, \quad \int_{\mathbb{S}^2} s_i s_j s_k \, d\boldsymbol{s} = 0, \quad \int_{\mathbb{S}^2} d\boldsymbol{s} = 4\pi. \quad (2.5a\text{--}d)
$$

Then, it is possible to make the link between the scalar function $f(t, \boldsymbol{x}, \boldsymbol{p}, \boldsymbol{s})$ and its zeroth- and first-order 'spin moments' $(f_0, \boldsymbol{f})(t, \boldsymbol{x}, \boldsymbol{p})$, defined by

$$
f_0 = \int_{\mathbb{S}^2} f \, d\boldsymbol{s}, \quad \boldsymbol{f} = 3 \int_{\mathbb{S}^2} \boldsymbol{s} f \, d\boldsymbol{s}. \quad (2.6a,b)
$$

Combining (2.3), (2.4) and (2.6*a,b*), we obtain the following relation between the scalar and vector representations:

$$
f(t, \boldsymbol{x}, \boldsymbol{p}, \boldsymbol{s}) = \frac{1}{4\pi}(f_0(t, \boldsymbol{x}, \boldsymbol{p}) + \boldsymbol{s} \cdot \boldsymbol{f}(t, \boldsymbol{x}, \boldsymbol{p})). \quad (2.7)
$$

Again, we note the linear relationship in the spin variable. We also note that $(f_0, \boldsymbol{f})$ are nothing but the components of the Wigner function $W_{\alpha, \beta}$ written in the Pauli basis, i.e. $f_0 = \text{Tr}(W)$, $\boldsymbol{f} = \text{Tr}(\boldsymbol{\sigma} W)$.

Then, the evolution equations for the vectorial model can be seen as the evolution equations for the 'spin moments' of the scalar distribution $f(t, \boldsymbol{x}, \boldsymbol{p}, \boldsymbol{s})$, which are obtained

by integrating (2.2) in spin space and assuming the relationship (2.7). This yields

$$
\begin{cases}
\dfrac{\partial f_0}{\partial t} + \boldsymbol{p} \cdot \nabla f_0 + (\boldsymbol{E} + \boldsymbol{p} \times \boldsymbol{B}) \cdot \dfrac{\partial f_0}{\partial \boldsymbol{p}} + \dfrac{(\beta + 2\gamma)\mathfrak{h}}{3} \sum_{j=1}^{3} \nabla B_j \cdot \nabla_{\boldsymbol{p}} f_j = 0, \\[3mm]
\dfrac{\partial f_j}{\partial t} + \boldsymbol{p} \cdot \nabla f_j + (\boldsymbol{E} + \boldsymbol{p} \times \boldsymbol{B}) \cdot \dfrac{\partial f_j}{\partial \boldsymbol{p}} + \beta\mathfrak{h} \nabla B_j \cdot \nabla_{\boldsymbol{p}} f_0 + (\boldsymbol{B} \times \boldsymbol{f})_j = 0, \quad j = 1, 2, 3, \\[3mm]
\dfrac{\partial \boldsymbol{E}}{\partial t} = \nabla \times \boldsymbol{B} - \left(\displaystyle\int_{\mathbb{R}^3} \boldsymbol{p} f_0 \mathrm{d}\boldsymbol{p} + \dfrac{\alpha\mathfrak{h}}{3} \nabla \times \displaystyle\int_{\mathbb{R}^3} \boldsymbol{f} \mathrm{d}\boldsymbol{p} \right), \\[3mm]
\dfrac{\partial \boldsymbol{B}}{\partial t} = -\nabla \times \boldsymbol{E}, \\[3mm]
\nabla \cdot \boldsymbol{E} = \rho - 1, \quad \rho = \displaystyle\int_{\mathbb{R}^3} f_0 \, \mathrm{d}\boldsymbol{p}, \quad \nabla \cdot \boldsymbol{B} = 0,
\end{cases}
\tag{2.8}
$$

with initial conditions

$$
\left.
\begin{aligned}
(f_0(t=0), \quad \boldsymbol{f}(t=0)) = (f_0^0, \boldsymbol{f}^0), \quad \nabla \cdot \boldsymbol{E}^0 = \int_{\mathbb{R}^3} f_0^0 \, \mathrm{d}\boldsymbol{p} - 1, \\[2mm]
\boldsymbol{B}(t=0) = \boldsymbol{B}^0 \text{ such that } \nabla \cdot \boldsymbol{B}^0 = 0.
\end{aligned}
\right\}
\tag{2.9a–d}
$$

However, as we shall see, the structure (2.7) is not satisfied for all times by the solution of the scalar model (2.2) for any arbitrary choice of α, β, γ. When this structure is not preserved by the time evolution, then the equivalence between the scalar model and its spin moments (which constitute the vector model) is not satisfied. Only for a particular choice of the parameters can one establish the equivalence, as stated in the following Proposition.

PROPOSITION 1. *$(f, \boldsymbol{E}, \boldsymbol{B})$ is a solution of the scalar model (2.2) (with $\gamma = \beta$ and $\alpha \in \mathbb{R}$) with initial condition (2.2a–c) with $f^0 = (1/4\pi)(f_0^0 + \boldsymbol{s} \cdot \boldsymbol{f}^0)$ if and only if $(f_0(t), \boldsymbol{f}(t))$ is a solution of the vector model (2.8) with the initial condition (2.9a–d).*

Proof. Assuming that the initial condition satisfies $f(t=0) = (1/4\pi)(f_0(t=0) + \boldsymbol{s} \cdot \boldsymbol{f}(t=0))$, we check that $f(t) = (1/4\pi)(f_0(t) + \boldsymbol{s} \cdot \boldsymbol{f}(t)) = (1/4\pi)(f_0(t) + \sum_i s_i f_i(t))$ is true for all time $t > 0$. To do so, we insert the decomposition $f(t) = (1/4\pi)(f_0(t) + \boldsymbol{s} \cdot \boldsymbol{f}(t))$ into the scalar equation (2.2). After some calculations detailed in Appendix A, we obtain

$$
\begin{aligned}
0 = {}& \frac{1}{4\pi} \frac{\partial (f_0 + \boldsymbol{s} \cdot \boldsymbol{f})}{\partial t} + \frac{1}{4\pi} \boldsymbol{p} \cdot \nabla (f_0 + \boldsymbol{s} \cdot \boldsymbol{f}) + \frac{1}{4\pi} (\boldsymbol{s} \times \boldsymbol{B}) \cdot \frac{\partial (f_0 + \boldsymbol{s} \cdot \boldsymbol{f})}{\partial \boldsymbol{s}} \\
& + \frac{1}{4\pi} \left[(\boldsymbol{E} + \boldsymbol{p} \times \boldsymbol{B}) + \beta\mathfrak{h} \nabla (\boldsymbol{s} \cdot \boldsymbol{B}) + \beta\mathfrak{h} \nabla \left(\boldsymbol{B} \cdot \frac{\partial}{\partial \boldsymbol{s}} \right) \right] \cdot \frac{\partial (f_0 + \boldsymbol{s} \cdot \boldsymbol{f})}{\partial \boldsymbol{p}} \\
= {}& \frac{1}{4\pi} \left(\frac{\partial f_0}{\partial t} + \boldsymbol{p} \cdot \nabla f_0 + (\boldsymbol{E} + \boldsymbol{p} \times \boldsymbol{B}) \cdot \frac{\partial f_0}{\partial \boldsymbol{p}} + \beta\mathfrak{h} \sum_i \nabla B_i \cdot \frac{\partial f_i}{\partial \boldsymbol{p}} \right) \\
& + \frac{1}{4\pi} \sum_i s_i \left(\frac{\partial f_i}{\partial t} + \boldsymbol{p} \cdot \nabla f_i + (\boldsymbol{E} + \boldsymbol{p} \times \boldsymbol{B}) \cdot \frac{\partial f_i}{\partial \boldsymbol{p}} + (\boldsymbol{B} \times \boldsymbol{f})_i + \beta\mathfrak{h} \nabla B_i \cdot \frac{\partial f_0}{\partial \boldsymbol{p}} \right).
\end{aligned}
\tag{2.10}
$$

Since $(1, s_1, s_2, s_3)$ is a basis, we can identify the coefficients to be zero which leads to the four equations of the vector model satisfied by (f_0, f_1, f_2, f_3). Thus, since f and $(1/4\pi)$ $(f_0 + s \cdot f)$ share the same initial condition, we get that $f = (1/4\pi)(f_0 + s \cdot f)$ is a solution of the scalar model if and only if (f_0, f_1, f_2, f_3) is the solution of vector model (2.8). $\qquad\square$

This Proposition provides a link between the vector and the scalar models, which implies that we can solve either a six-dimensional phase space vector model or an extended nine-dimensional scalar model. Let us remark that the additional term (preceded by the coefficient γ) is not easy to approximate using PIC methods, since it is a second-order cross-derivative term, whereas its counterpart in the vector model is a simple transport term.

2.1.3. *Poisson structure*

It has been shown in (Marklund & Morrison 2011) (see also Qin *et al.* 2015; Xiao *et al.* 2015) that the scalar model (2.2) with $\gamma = 0$, $\alpha = \beta$ enjoys a non-canonical Poisson structure with the following Poisson bracket:

$$
\begin{aligned}
\{\mathcal{F}, \mathcal{G}\} = &\int f \left[\frac{\delta\mathcal{F}}{\delta f}, \frac{\delta\mathcal{G}}{\delta f} \right]_{xp} \mathrm{d}x\,\mathrm{d}p\,\mathrm{d}s + \int \left(\frac{\delta\mathcal{F}}{\delta E} \cdot \frac{\partial f}{\partial p}\frac{\delta\mathcal{G}}{\delta f} - \frac{\delta\mathcal{G}}{\delta E} \cdot \frac{\partial f}{\partial p}\frac{\delta\mathcal{F}}{\delta f} \right) \mathrm{d}x\,\mathrm{d}p\,\mathrm{d}s \\
&+ \int \left(\frac{\delta\mathcal{F}}{\delta E} \cdot \left(\triangledown \times \frac{\delta\mathcal{G}}{\delta B} \right) - \frac{\delta\mathcal{G}}{\delta E} \cdot \left(\triangledown \times \frac{\delta\mathcal{F}}{\delta B} \right) \right) \mathrm{d}x \\
&+ \int f B \cdot \left(\frac{\partial}{\partial p}\frac{\delta\mathcal{F}}{\delta f} \times \frac{\partial}{\partial p}\frac{\delta\mathcal{G}}{\delta f} \right) \mathrm{d}x\,\mathrm{d}p\,\mathrm{d}s \\
&+ \frac{1}{\beta\hbar} \int f s \cdot \left(\frac{\partial}{\partial s}\frac{\delta\mathcal{F}}{\delta f} \times \frac{\partial}{\partial s}\frac{\delta\mathcal{G}}{\delta f} \right) \mathrm{d}x\,\mathrm{d}p\,\mathrm{d}s,
\end{aligned}
\tag{2.11}
$$

and the Hamiltonian functional

$$
\mathcal{H}(f, E, B) = \frac{1}{2} \int |p|^2 f\,\mathrm{d}x\,\mathrm{d}p\,\mathrm{d}s - \beta\hbar \int s \cdot B f\,\mathrm{d}x\,\mathrm{d}p\,\mathrm{d}s + \frac{1}{2} \int \left(|E|^2 + |B|^2 \right) \mathrm{d}x,
\tag{2.12}
$$

so that the scalar model can be reformulated as $\partial_t \mathcal{Z} = \{\mathcal{Z}, \mathcal{H}\}$, with $\mathcal{Z} = (f, E, B)$.

We can also construct a geometric Poisson structure for the vector model introduced in Hurst *et al.* (2014, 2017). For that, we need $\beta + 2\gamma = \alpha$ in (2.8) and the Poisson bracket is

$$
\begin{aligned}
\{\mathcal{F}, \mathcal{G}\} = &\int f_0 \left[\frac{\delta\mathcal{F}}{\delta f_0}, \frac{\delta\mathcal{G}}{\delta f_0} \right] \mathrm{d}x\,\mathrm{d}p + \sum_{i=1}^{3} \int f_i \left[\frac{\delta\mathcal{F}}{\delta f_i}, \frac{\delta\mathcal{G}}{\delta f_0} \right] \mathrm{d}x\,\mathrm{d}p \\
&+ \sum_{i=1}^{3} \int f_i \left[\frac{\delta\mathcal{F}}{\delta f_0}, \frac{\delta\mathcal{G}}{\delta f_i} \right] \mathrm{d}x\,\mathrm{d}p + \sum_{i=1}^{3} \frac{3\beta}{\alpha} \int f_0 \left[\frac{\delta\mathcal{F}}{\delta f_i}, \frac{\delta\mathcal{G}}{\delta f_i} \right] \mathrm{d}x\,\mathrm{d}p \\
&+ \sum_{i=0}^{3} \int \left(\frac{\delta\mathcal{F}}{\delta E} \cdot \frac{\partial f_i}{\partial p}\frac{\delta\mathcal{G}}{\delta f_i} - \frac{\delta\mathcal{G}}{\delta E} \cdot \frac{\partial f_i}{\partial p}\frac{\delta\mathcal{F}}{\delta f_i} \right) \mathrm{d}x\,\mathrm{d}p \\
&+ \int f_0 B \cdot \left(\frac{\partial}{\partial p}\frac{\delta\mathcal{F}}{\delta f_0} \times \frac{\partial}{\partial p}\frac{\delta\mathcal{G}}{\delta f_0} \right) \mathrm{d}x\,\mathrm{d}p
\end{aligned}
$$

$$+ \sum_{i=1}^{3} \int f_i \boldsymbol{B} \cdot \left(\frac{\partial}{\partial \boldsymbol{p}} \frac{\delta \mathcal{F}}{\delta f_i} \times \frac{\partial}{\partial \boldsymbol{p}} \frac{\delta \mathcal{G}}{\delta f_0} - \frac{\partial}{\partial \boldsymbol{p}} \frac{\delta \mathcal{F}}{\delta f_0} \times \frac{\partial}{\partial \boldsymbol{p}} \frac{\delta \mathcal{G}}{\delta f_i} \right) \mathrm{d}\boldsymbol{x}\, \mathrm{d}\boldsymbol{p}$$

$$+ \frac{3}{\alpha} \frac{1}{\hbar} \int \boldsymbol{f} \cdot \left(\frac{\delta \mathcal{F}}{\delta \boldsymbol{f}} \times \frac{\delta \mathcal{G}}{\delta \boldsymbol{f}} \right) \mathrm{d}\boldsymbol{x}\, \mathrm{d}\boldsymbol{p}$$

$$+ \int \left(\frac{\delta \mathcal{F}}{\delta \boldsymbol{E}} \cdot \left(\triangledown \times \frac{\delta \mathcal{G}}{\delta \boldsymbol{B}} \right) - \frac{\delta \mathcal{G}}{\delta \boldsymbol{E}} \cdot \left(\triangledown \times \frac{\delta \mathcal{F}}{\delta \boldsymbol{B}} \right) \right) \mathrm{d}\boldsymbol{x}, \tag{2.13}$$

while the Hamiltonian functional is

$$\mathcal{H}(f_0, \boldsymbol{f}, \boldsymbol{E}, \boldsymbol{B}) = \frac{1}{2} \int |\boldsymbol{p}|^2 f_0 \, \mathrm{d}\boldsymbol{x}\, \mathrm{d}\boldsymbol{p} + \frac{1}{2} \int \left(|\boldsymbol{E}|^2 + |\boldsymbol{B}|^2 \right) \mathrm{d}\boldsymbol{x} - \frac{\alpha}{3} \hbar \int \boldsymbol{B} \cdot \boldsymbol{f} \, \mathrm{d}\boldsymbol{x}\, \mathrm{d}\boldsymbol{p}, \tag{2.14}$$

so that the system can be written as $\partial_t \mathcal{Z} = \{\mathcal{Z}, \mathcal{H}\}$. It is easy to check that this bracket is bilinear, skew-symmetric and verifies Leibniz's rule, but it is not clear whether the Jacobi identity is satisfied. Hence, this bracket is not strictly speaking a Poisson bracket such as the one occurring in the scalar model; nevertheless, we will still refer to it as a Poisson bracket for the sake of simplicity. We note that the case $\beta = 1$, $\gamma = 1$ and $\alpha = 3$ yields the vector model introduced in (Hurst *et al.* 2014, 2017; Manfredi *et al.* 2022) and ensures, by Proposition 1, the equivalence between the two models.

2.1.4. *Summary*

In summary, we have found that, in order to ensure the equivalence between the scalar model (2.2) and the vector model (2.8), one needs to take $\beta = \gamma$ and arbitrary α. Furthermore, the vector model enjoys a geometric (antisymmetric-bracket) structure when $\beta + 2\gamma = \alpha$. The choice $\beta = 1$, $\gamma = 1$ and $\alpha = 3$ satisfies both conditions, and recovers the 'standard' vector model commonly used in the literature (Hurst *et al.* 2014, 2017; Manfredi *et al.* 2022). However, as the γ-term is difficult to implement in a PIC method because of the double derivative, it has been common to take $\gamma = 0$ when simulating the scalar model (Crouseilles *et al.* 2021). In that case, it is still possible to recover the Poisson structure when $\alpha = \beta$, but the equivalence with the standard vectorial model no longer holds.

2.2. *Reduced 1-D scalar and vector models*

Here, we develop a reduced 1-D model that is relevant to study laser–plasma interactions. Both scalar and vector models are considered.

2.2.1. *The 1-D scalar model*

Following Ghizzo *et al.* (1990), Crouseilles *et al.* (2021) and Manfredi *et al.* (2022), one can derive a reduced 1-D spin-Vlasov–Maxwell model by considering the case of a plasma interacting with an electromagnetic wave propagating in the longitudinal x direction and assuming that all fields depend spatially on x only. Choosing the Coulomb gauge $\boldsymbol{\nabla} \cdot \boldsymbol{A} = 0$, the vector potential $\boldsymbol{A}$ lies in the perpendicular (transverse) plane, i.e. $\boldsymbol{A} = (0, A_y, A_z) = (0, \boldsymbol{A}_\perp)$. Using $\boldsymbol{E} = -\boldsymbol{\nabla}\phi - \partial_t \boldsymbol{A}$, we obtain, using the notation $\boldsymbol{E} = (E_x, E_y, E_z) = (E_x, \boldsymbol{E}_\perp)$: $\boldsymbol{E}_\perp = -\partial_t \boldsymbol{A}_\perp$ and $E_x = -\partial_x \phi$, and $\boldsymbol{B} = \boldsymbol{\nabla} \times \boldsymbol{A} = (0, -\partial_x A_z, \partial_x A_y)$. We then consider an electron distribution that is 'cold' in the transverse plane, i.e. $\delta(\boldsymbol{p}_\perp - \boldsymbol{A}_\perp) f(t, x, p_x, \boldsymbol{s})$, where $\boldsymbol{p} = (p_x, p_y, p_z) = (p_x, \boldsymbol{p}_\perp)$ is the linear momentum and $\boldsymbol{p} - \boldsymbol{A}$ is the canonical momentum. After integration with respect to $\boldsymbol{p}_\perp$, the relevant extended phase space is reduced to five dimensions, instead of nine dimensions for the general case. in the following, the longitudinal variable p_x will be simply denoted by p.

The scalar spin-Vlasov–Maxwell system (2.2) becomes

$$
\left\{
\begin{aligned}
&\frac{\partial f}{\partial t} + p\frac{\partial f}{\partial x} + \left[E_x - \boldsymbol{A}_\perp \cdot \frac{\partial \boldsymbol{A}_\perp}{\partial x} - \mathfrak{h}\frac{\partial^2 A_z}{\partial x^2}\left(\beta s_2 + \gamma\frac{\partial}{\partial s_2} \right) + \mathfrak{h}\frac{\partial^2 A_y}{\partial x^2}\left(\beta s_3 + \gamma\frac{\partial}{\partial s_3} \right) \right]\frac{\partial f}{\partial p} \\
&\qquad + \left[s_3\frac{\partial A_z}{\partial x} + s_2\frac{\partial A_y}{\partial x}, -s_1\frac{\partial A_y}{\partial x}, -s_1\frac{\partial A_z}{\partial x} \right]\cdot\frac{\partial f}{\partial \boldsymbol{s}} = 0, \\
&\qquad\qquad\qquad \frac{\partial E_x}{\partial t} = -\int_{\mathbb{R}^4} pf\,\mathrm{d}p\,\mathrm{d}\boldsymbol{s}, \\
&\frac{\partial E_y}{\partial t} = -\frac{\partial^2 A_y}{\partial x^2} + A_y\int_{\mathbb{R}^4} f\,\mathrm{d}p\,\mathrm{d}\boldsymbol{s} + \alpha\mathfrak{h}\int_{\mathbb{R}^4} s_3\frac{\partial f}{\partial x}\mathrm{d}p\,\mathrm{d}\boldsymbol{s}, \\
&\frac{\partial E_z}{\partial t} = -\frac{\partial^2 A_z}{\partial x^2} + A_z\int_{\mathbb{R}^4} f\,\mathrm{d}p\,\mathrm{d}\boldsymbol{s} - \alpha\mathfrak{h}\int_{\mathbb{R}^4} s_2\frac{\partial f}{\partial x}\mathrm{d}p\,\mathrm{d}\boldsymbol{s}, \\
&\qquad\qquad\qquad \frac{\partial \boldsymbol{A}_\perp}{\partial t} = -\boldsymbol{E}_\perp, \\
&\qquad\qquad\qquad \frac{\partial E_x}{\partial x} = \int_{\mathbb{R}^4} f\,\mathrm{d}p\,\mathrm{d}\boldsymbol{s} - 1,
\end{aligned}
\right.
\tag{2.15}
$$

with initial condition

$$
\left.
\begin{aligned}
f(t=0) &= f^0, \quad \frac{\partial E_x^0}{\partial x} = \int_{\mathbb{R}^4} f^0\,\mathrm{d}p\,\mathrm{d}\boldsymbol{s} - 1, \\
(E_y, E_z)(t=0) &= (E_y^0, E_z^0), \quad \boldsymbol{A}_\perp(t=0) = \boldsymbol{A}_\perp^0.
\end{aligned}
\right\}
\tag{2.16a–d}
$$

Taking $\gamma = 0$ and $\alpha = \beta$, the scalar spin-Vlasov–Maxwell system (2.15) can be expressed with one Poisson bracket as follows. For any two functionals $\mathcal{F}$, and $\mathcal{G}$ depending on f, $\boldsymbol{E}$ and $\boldsymbol{A}_\perp$, we have

$$
\begin{aligned}
\{\mathcal{F}, \mathcal{G}\} &= \int f\left[\frac{\delta\mathcal{F}}{\delta f}, \frac{\delta\mathcal{G}}{\delta f} \right]_{xp} \mathrm{d}x\,\mathrm{d}p\,\mathrm{d}\boldsymbol{s} + \int\left(\frac{\delta\mathcal{F}}{\delta E_x}\frac{\partial f}{\partial p}\frac{\delta\mathcal{G}}{\delta f} - \frac{\delta\mathcal{G}}{\delta E_x}\frac{\partial f}{\partial p}\frac{\delta\mathcal{F}}{\delta f} \right)\mathrm{d}x\,\mathrm{d}p\,\mathrm{d}\boldsymbol{s} \\
&\quad + \int\left(\frac{\delta\mathcal{G}}{\delta\boldsymbol{A}_\perp}\cdot\frac{\delta\mathcal{F}}{\delta\boldsymbol{E}_\perp} - \frac{\delta\mathcal{F}}{\delta\boldsymbol{A}_\perp}\cdot\frac{\delta\mathcal{G}}{\delta\boldsymbol{E}_\perp} \right)\mathrm{d}x \\
&\quad + \frac{1}{\beta\mathfrak{h}}\int f\boldsymbol{s}\cdot\left(\frac{\partial}{\partial\boldsymbol{s}}\frac{\delta\mathcal{F}}{\delta f} \times \frac{\partial}{\partial\boldsymbol{s}}\frac{\delta\mathcal{G}}{\delta f} \right)\mathrm{d}x\,\mathrm{d}p\,\mathrm{d}\boldsymbol{s}.
\end{aligned}
\tag{2.17}
$$

With the Hamiltonian functional defined by

$$
\begin{aligned}
\mathcal{H}(f, \boldsymbol{E}, \boldsymbol{A}_\perp) &= \frac{1}{2}\int p^2 f\,\mathrm{d}x\,\mathrm{d}p\,\mathrm{d}\boldsymbol{s} + \frac{1}{2}\int |\boldsymbol{A}_\perp|^2 f\,\mathrm{d}x\,\mathrm{d}p\,\mathrm{d}\boldsymbol{s} \\
&\quad + \frac{1}{2}\int\left(|\boldsymbol{E}|^2 + \left| \frac{\partial\boldsymbol{A}_\perp}{\partial x} \right|^2 \right)\mathrm{d}x + \beta\mathfrak{h}\int\left(s_2\frac{\partial A_z}{\partial x} - s_3\frac{\partial A_y}{\partial x} \right)f\,\mathrm{d}x\,\mathrm{d}p\,\mathrm{d}\boldsymbol{s},
\end{aligned}
\tag{2.18}
$$

the scalar spin Vlasov–Maxwell system of equations (2.15) can thus be reformulated as $\partial_t\mathcal{Z} = \{\mathcal{Z}, \mathcal{H}\}$, where $\mathcal{Z} = (f, E_x, E_y, E_z, A_y, A_z)$ denotes the vector of the dynamical variables.

2.2.2. *The 1-D vector model*

Here, the goal is to derive an equivalent model of (2.15) satisfied by $(f_0, \boldsymbol{f})(t, x, p)$. To do so, we use Proposition 1 which states that the scalar model is equivalent to the vector model whose unknown are given by some moments in the $\boldsymbol{s}$ variable. We now state the following Proposition 2, which is adapted to the 1-D laser–plasma model we consider here. Proposition 2 is a direct consequence of Proposition 1, hence the derivation of the vector model is postponed to Appendix B.

PROPOSITION 2. *Let $f(t)$ the solution to the scalar model* (2.15) *(with $\gamma = \beta$ and $\alpha \in \mathbb{R}$) with initial conditions* (2.16a–d) *with $f^0 = (1/4\pi)(f_0^0 + \boldsymbol{s} \cdot \boldsymbol{f}^0)$. Then, $(f_0(t), \boldsymbol{f}(t))$ is the solution of the following vector model where $\boldsymbol{B} = (0, -\partial_x A_z, \partial_x A_y)$:*

$$
\begin{cases}
\dfrac{\partial f_0}{\partial t} + p\dfrac{\partial f_0}{\partial x} + \left(E_x - \boldsymbol{A}_\perp \cdot \dfrac{\partial \boldsymbol{A}_\perp}{\partial x}\right)\dfrac{\partial f_0}{\partial p} - \dfrac{(\beta + 2\gamma)}{3}\mathfrak{h}\dfrac{\partial^2 A_z}{\partial x^2}\dfrac{\partial f_2}{\partial p} + \beta\mathfrak{h}\dfrac{\partial^2 A_y}{\partial x^2}\dfrac{\partial f_3}{\partial p} = 0, \\[2ex]
\dfrac{\partial \boldsymbol{f}}{\partial t} + p\dfrac{\partial \boldsymbol{f}}{\partial x} + \left(E_x - \boldsymbol{A}_\perp \cdot \dfrac{\partial \boldsymbol{A}_\perp}{\partial x}\right)\dfrac{\partial \boldsymbol{f}}{\partial p} + \boldsymbol{B} \times \boldsymbol{f} + \beta\mathfrak{h}\dfrac{\partial \boldsymbol{B}}{\partial x}\dfrac{\partial f_0}{\partial p} = 0, \\[2ex]
\dfrac{\partial E_x}{\partial t} = -\displaystyle\int_{\mathbb{R}} pf_0 \, \mathrm{d}p, \\[2ex]
\dfrac{\partial E_y}{\partial t} = -\dfrac{\partial^2 A_y}{\partial x^2} + A_y\displaystyle\int_{\mathbb{R}} f_0 \, \mathrm{d}p + \dfrac{\alpha\mathfrak{h}}{3}\displaystyle\int_{\mathbb{R}}\dfrac{\partial f_3}{\partial x}\mathrm{d}p, \\[2ex]
\dfrac{\partial E_z}{\partial t} = -\dfrac{\partial^2 A_z}{\partial x^2} + A_z\displaystyle\int_{\mathbb{R}} f_0 \, \mathrm{d}p - \dfrac{\alpha\mathfrak{h}}{3}\displaystyle\int_{\mathbb{R}}\dfrac{\partial f_2}{\partial x}\mathrm{d}p, \\[2ex]
\dfrac{\partial \boldsymbol{A}_\perp}{\partial t} = -\boldsymbol{E}_\perp, \\[2ex]
\dfrac{\partial E_x}{\partial x} = \displaystyle\int_{\mathbb{R}} f_0 \, \mathrm{d}p - 1,
\end{cases}
\tag{2.19}
$$

with the initial conditions $(f_0(t = 0), \boldsymbol{f}(t = 0)) = (f_0^0, \boldsymbol{f}^0)$, $\partial E_x/\partial x = \int_{\mathbb{R}} f_0^0 \, \mathrm{d}p - 1$, $(E_y, E_z)(t = 0) = (E_y^0, E_z^0)$, $\boldsymbol{A}_\perp(t = 0) = \boldsymbol{A}_\perp^0$. Conversely, if $(f_0(t), \boldsymbol{f}(t))$ is the solution of (2.19), *thus $f(t) = (1/4\pi)(f_0(t) + \boldsymbol{s} \cdot \boldsymbol{f}(t))$ is the solution of the scalar model* (2.15) *(with $\gamma = \beta, \alpha \in \mathbb{R}$).*

2.2.3. *Poisson structure*

The model (2.19) with $\alpha = \beta + 2\gamma$ enjoys a Poisson structure with the following (antisymmetric) bracket:

$$
\{\mathcal{F}, \mathcal{G}\} = \int f_0\left[\dfrac{\delta\mathcal{F}}{\delta f_0}, \dfrac{\delta\mathcal{G}}{\delta f_0}\right]_{xp} \mathrm{d}x\,\mathrm{d}p + \sum_{i=1}^{3}\int f_i\left[\dfrac{\delta\mathcal{F}}{\delta f_0}, \dfrac{\delta\mathcal{G}}{\delta f_i}\right]_{xp} \mathrm{d}x\,\mathrm{d}p
$$

$$
+ \sum_{i=1}^{3}\int f_i\left[\dfrac{\delta\mathcal{F}}{\delta f_i}, \dfrac{\delta\mathcal{G}}{\delta f_0}\right]_{xp} \mathrm{d}x\,\mathrm{d}p
$$

$$
+ \dfrac{3\beta}{\alpha}\sum_{i=1}^{3}\int f_0\left[\dfrac{\delta\mathcal{F}}{\delta f_i}, \dfrac{\delta\mathcal{G}}{\delta f_i}\right]_{xp} \mathrm{d}x\,\mathrm{d}p
$$

$$+ \sum_{i=0}^{3} \int \left(\frac{\delta \mathcal{F}}{\delta E_x} \frac{\partial f_i}{\partial p} \frac{\delta \mathcal{G}}{\delta f_i} - \frac{\delta \mathcal{G}}{\delta E_x} \frac{\partial f_i}{\partial p} \frac{\delta \mathcal{F}}{\delta f_i} \right) dx \, dp$$

$$+ \frac{3}{\alpha \hbar} \int f \cdot \left(\frac{\delta \mathcal{F}}{\delta f} \times \frac{\delta \mathcal{G}}{\delta f} \right) dx \, dp + \int \left(\frac{\delta \mathcal{G}}{\delta A_\perp} \cdot \frac{\delta \mathcal{F}}{\delta E_\perp} - \frac{\delta \mathcal{F}}{\delta A_\perp} \cdot \frac{\delta \mathcal{G}}{\delta E_\perp} \right) dx, \tag{2.20}$$

where $f = (f_1, f_2, f_3)$. The Hamiltonian functional is given by

$$\mathcal{H}(f_0, f, E, A_\perp) = \frac{1}{2} \int p^2 f_0 \, dx \, dp + \frac{1}{2} \int |A_\perp|^2 f_0 \, dx \, dp$$

$$+ \frac{1}{2} \int \left(|E|^2 + \left| \frac{\partial A_\perp}{\partial x} \right|^2 \right) dx + \frac{\alpha \hbar}{3} \int \left(f_2 \frac{\partial A_z}{\partial x} - f_3 \frac{\partial A_y}{\partial x} \right) dx \, dp, \tag{2.21}$$

so that the system can be written in a compact form as

$$\frac{\partial \mathcal{Z}}{\partial t} = \{\mathcal{Z}, \mathcal{H}\}, \tag{2.22}$$

where $\mathcal{Z} = (f_0, f, E_x, E_y, E_z, A_y, A_z)$ denotes the vector of the dynamical variables.

2.3. *Discretization of the 1-D vector model*

Here, we present the numerical method that we shall use to compute an approximate solution of (2.19). Regarding the time discretization, we use a Hamiltonian splitting method which provides a way to split the terms of the partial differential equation system (2.19). For the phase-space discretization, spectral methods are used in space, while finite-volume methods are used for the velocity direction.

For the system (2.19), the Hamiltonian (2.21) can be split into five parts,

$$\mathcal{H} = \mathcal{H}_p + \mathcal{H}_A + \mathcal{H}_E + \mathcal{H}_2 + \mathcal{H}_3, \tag{2.23}$$

where

$$\left. \begin{aligned} \mathcal{H}_p = \frac{1}{2} \int p^2 f_0 \, dx \, dp, \quad \mathcal{H}_A = \frac{1}{2} \int |A_\perp|^2 f_0 \, dx \, dp + \frac{1}{2} \int \left| \frac{\partial A_\perp}{\partial x} \right|^2 dx, \\ \mathcal{H}_E = \frac{1}{2} \int |E|^2 \, dx = \frac{1}{2} \int (E_x^2 + |E_\perp|^2) \, dx, \\ \mathcal{H}_2 = \frac{\alpha \hbar}{3} \int f_2 \frac{\partial A_z}{\partial x} dx \, dp, \quad \mathcal{H}_3 = -\frac{\alpha \hbar}{3} \int f_3 \frac{\partial A_y}{\partial x} dx \, dp. \end{aligned} \right\} \tag{2.24}$$

With (2.22) and (2.23), we split the Hamiltonian to get

$$\frac{\partial \mathcal{Z}}{\partial t} = \{\mathcal{Z}, \mathcal{H}_p\} + \{\mathcal{Z}, \mathcal{H}_A\} + \{\mathcal{Z}, \mathcal{H}_E\} + \{\mathcal{Z}, \mathcal{H}_2\} + \{\mathcal{Z}, \mathcal{H}_3\}, \tag{2.25}$$

which induces five subsystems to solve: $\partial_t \mathcal{Z} = \{\mathcal{Z}, \mathcal{H}_\star\}$ with $\star = p, A, E, 2, 3$ according to (2.23). Denoting $\varphi_t^{\mathcal{H}_\star}(\mathcal{Z}(0))$ the exact solution at time t of $\partial_t \mathcal{Z} = \{\mathcal{Z}, \mathcal{H}_\star\}$ with the initial
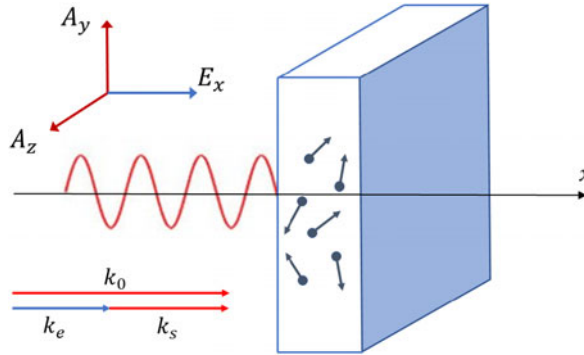
FIGURE 1. Schematic view of the geometry of the laser–plasma interaction during stimulated Raman scattering. The electromagnetic vector potential lies in the transverse plane (y, z), whereas the electrostatic field is directed along the longitudinal direction x, which is the direction of propagation of the electromagnetic wave. Here k_0, k_s and k_e represent the wavenumbers for the incident wave, the scattered wave and the electron plasma wave, respectively.

condition $\mathcal{Z}(0)$, the solution of the full model (2.22) is thus approximated by

$$\mathcal{Z}(t) = (\Pi_{\star=p,A,E,2,3}\, \varphi_t^{\mathcal{H}_\star})\mathcal{Z}(0). \tag{2.26}$$

This is a first-order splitting, but higher-order ones can also be derived. Since the splitting involves here five steps, we will restrict ourselves to the Strang scheme

$$\mathcal{Z}(t) = (\varphi_{t/2}^{\mathcal{H}_p} \circ \varphi_{t/2}^{\mathcal{H}_A} \circ \varphi_{t/2}^{\mathcal{H}_E} \circ \varphi_{t/2}^{\mathcal{H}_2} \circ \varphi_t^{\mathcal{H}_3} \circ \varphi_{t/2}^{\mathcal{H}_2} \circ \varphi_{t/2}^{\mathcal{H}_E} \circ \varphi_{t/2}^{\mathcal{H}_A} \circ \varphi_{t/2}^{\mathcal{H}_p})\mathcal{Z}(0). \tag{2.27}$$

The details of the calculations of the subsystem solutions are given in Appendix C. It turns out that each subsystem $\partial_t \mathcal{Z} = \{\mathcal{Z}, \mathcal{H}_\star\}$ with $\star = p, A, E, 2, 3$ can be solved exactly in time so that the error in time only comes from the splitting itself, and can be controlled by using high-order schemes.

3. Numerical experiments

This section is dedicated to numerical simulations of the laser–plasma models presented above. Laser–plasma interactions are a broadly studied topic in plasma physics. An important problem in this field is the acceleration of charged particles by large amplitude plasma waves, which may be created, amongst others, through stimulated Raman scattering (SRS) (Forslund, Kindel & Lindman 1975). During SRS, an incident electromagnetic wave generates a scattered electromagnetic wave and a Langmuir plasma wave that accelerates the electrons (see figure 1). Here, our goal is to investigate the effect of the electron spin on the SRS instability through the simulation of the vectorial spin-Vlasov–Maxwell model (2.19) by using the grid-based (Eulerian) time-splitting method described in the preceding section.

Our analysis will proceed step by step. First, we consider the problem without spin, which has been studied in several earlier works (Ghizzo *et al.* 1990; Huot *et al.* 2003; Li *et al.* 2020) (§ 3.1). Second, we compare the results obtained with the scalar and vector models at short times, for different values of the scaled Planck constant $\hbar$ (§ 3.2.1). Next, we remove the effect of plasma self-consistency on the propagation of the electromagnetic wave, in order to precisely validate the numerical simulations for long times (§ 3.2.2). Finally, we simulate the general spin-dependent vector model for $\gamma = 0$ and 1 (which

corresponds to $\alpha = 1$ and 3, respectively) and check its conservation properties and other physical issues (§ 3.2.3).

3.1. *Stimulated Raman Scattering without spin*

We consider the model corresponding to (2.19) with $f = 0$ and $\mathfrak{h} = 0$ (which is the model studied in Ghizzo *et al.* 1990; Li *et al.* 2020). We use a perturbed Maxwellian as initial condition for f_0,

$$f_0(t = 0, x, p) = (1 + \epsilon \cos(k_e x)) \frac{1}{\sqrt{2\pi} v_{\text{th}}} \exp\left(-\frac{p^2}{2v_{\text{th}}^2}\right), \tag{3.1}$$

and the initial longitudinal electric field $E_x(t = 0, x) = (\epsilon/k_e) \sin(k_e x)$. Here, ϵ and k_e are the amplitude and the wavenumber of the perturbation, respectively, and v_{th} is the electron thermal speed (normalized to c). For the transverse fields, we consider an incident electromagnetic wave with circular polarization,

$$\left.\begin{array}{cc} E_y(t = 0, x) = E_0 \cos(k_0 x), & E_z(t = 0, x) = E_0 \sin(k_0 x), \\[2mm] A_y(t = 0, x) = -\dfrac{E_0}{\omega_0} \sin(k_0 x), & A_z(t = 0, x) = \dfrac{E_0}{\omega_0} \cos(k_0 x), \end{array}\right\} \tag{3.2}$$

where k_0, ω_0 and E_0 are the wavenumber, frequency and amplitude of the transverse electric field, respectively. We consider periodic boundary conditions with spatial period $L = 4\pi/k_e$, and take $p_{\max} = 5$ for the computational domain in momentum space. A schematic view of the geometry is shown in figure 1.

The dispersion relation can be derived from the usual matching conditions for frequency and wavenumber,

$$\omega_0 = \omega_s + \omega_e, \quad k_0 = k_s + k_e \tag{3.3a,b}$$

and

$$\omega_{0,s}^2 = 1 + k_{0,s}^2, \quad \omega_e^2 = 1 + 3k_e^2 v_{\text{th}}^2, \tag{3.4a,b}$$

where the subscript '0' refers to the pump wave, 's' to the scattered electromagnetic wave and 'e' to the electron plasma wave. As in Ghizzo *et al.* (1990), we take the following values for the above parameters:

$$\epsilon = 0.02, \quad k_e = 1.223, \quad k_0 = 2k_e, \quad v_{\text{th}} = 0.17. \tag{3.5a–d}$$

Then, using the matching relations (3.3a,b) and (3.4a,b), we get

$$\omega_0 = 2.643, \quad k_s = k_e, \quad \omega_s = 1.58, \quad \omega_e = 1.063. \tag{3.6a–d}$$

Finally, we take the amplitude of the incident wave $E_0 = E_{\text{ref}} = 0.325$ as a reference value.

To check the accuracy of our code in the spinless regime, the grid parameters are taken as $N_x = 129$, $N_p = 129$, $\Delta t = 0.05$ and a Strang splitting method is used for the time discretization. As we can observe in figure 2(a,b), the code preserves the total energy to very high precision (the relative error is less than 0.05 %).

We also consider the Poisson equation conservation; to do so, we define the quantity Poi.err as

$$\text{Poi.err}(t) = \left(\sum_k \left| \frac{2\pi \mathrm{i} k}{L} \hat{E}_{x,k}(t) - \Delta p \sum_{l=1}^{N_p} \hat{f}_{k,l}(t) \right|^2 \right)^{1/2}, \tag{3.7}$$

where $\hat{E}_{x,k}(t)$ is the kth Fourier component of the longitudinal electric field E_x, and $\hat{f}_{k,l}(t)$ is the kth Fourier component of the distribution function $f(x, p, t)$ computed at the lth grid
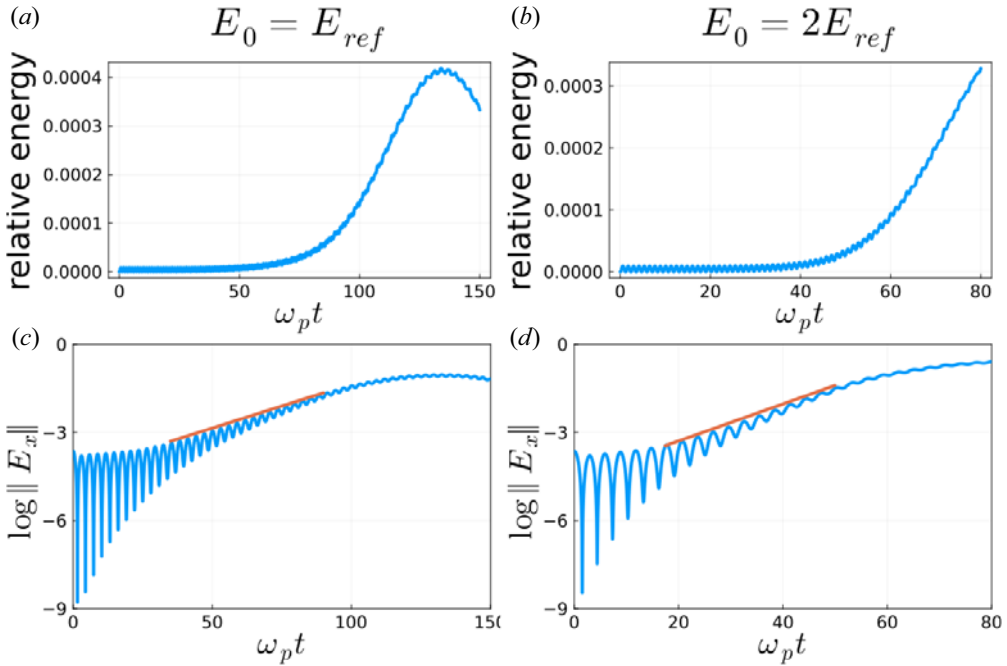
FIGURE 2. The SRS simulations without spin. Time evolution of the relative energy $|E_{tot}(t) - E_{tot}(0)|/E_{tot}(0)$ (a,b) and of the longitudinal electric field norm $\|E_x(t)\|$ in semilog scale (c,d), for $E_0 = E_{\mathrm{ref}} = 0.325$ (a,c) and $E_0 = 2E_{\mathrm{ref}} = 0.65$ (b,d). The red straight lines represent the instability growth rate expected from linear theory.

point in momentum space. If Poisson's equation is satisfied, the above quantity should vanish. We observe, as expected, that the Poisson equation conservation is ensured at the machine precision level. In figure 2(c,d), we also plot the time evolution of the longitudinal electric field norm

$$\|E_x(t)\| = \left(\frac{1}{2} \int_0^L E_x^2(t, x) \, \mathrm{d}x \right)^{1/2} \tag{3.8}$$

in semilog scale, for two values of the incident amplitude ($E_0 = E_{\mathrm{ref}} = 0.325$ and $E_0 = 2E_{\mathrm{ref}} = 0.65$). We observe that the instability growth rate ($\gamma_{\mathrm{inst}} \approx 0.03$ for $E_0 = E_{\mathrm{ref}}$ and $\gamma_{\mathrm{inst}} \approx 0.06$ for $E_0 = 2E_{\mathrm{ref}}$) is proportional to the amplitude E_0 and close to the value expected from the linear theory (Ghizzo *et al.* 1990).

3.2. *Vector and scalar models with spin*

Here, several comparisons are performed between the vector and scalar models in different configurations, but always with $\alpha = \beta = 1$ and $\gamma = 0$. Indeed, when $\gamma \neq 0$ the PIC code could not be used because of the double derivative in $\boldsymbol{p}$ and $\boldsymbol{s}$ in the Vlasov equation. We recall that the other condition ($\alpha = \beta = 1$) ensures the Poisson structure for the PIC method. However, as pointed out earlier, with this choice the scalar and vector models are not mathematically equivalent. Hence, any observed differences in the results may originate from either this inequivalence or from the different numerical method employed in the simulations (PIC or Eulerian).

We use the following initial conditions for the scalar model:

$$f(t = 0, x, p, s) = \frac{1}{4\pi}(1 + \eta s_z)(1 + \epsilon \cos(k_e x)) \frac{1}{\sqrt{2\pi} v_{\mathrm{th}}} \exp\left(-\frac{p^2}{2v_{\mathrm{th}}^2}\right), \qquad (3.9)$$

and for the vector model

$$\left.\begin{aligned}
f_0(t = 0, x, p) &= (1 + \epsilon \cos(k_e x)) \frac{1}{\sqrt{2\pi} v_{\mathrm{th}}} \exp\left(-\frac{p^2}{2v_{\mathrm{th}}^2}\right), \\
f_1(t = 0, x, p) &= f_2(t = 0, x, p) = 0, \\
f_3(t = 0, x, p) &= \frac{\eta}{3}(1 + \epsilon \cos(k_e x)) \frac{1}{\sqrt{2\pi} v_{\mathrm{th}}} \exp\left(-\frac{p^2}{2v_{\mathrm{th}}^2}\right),
\end{aligned}\right\} \qquad (3.10)$$

with $x \in [0, 4\pi/k_e]$, $p \in \mathbb{R}$, $s \in \mathbb{S}^2$. The variable η represents the degree of spin polarization of the electron gas (Manfredi *et al.* 2019): $\eta = 0$ for an unpolarized electron gas and $\eta = 1$ for a fully polarized one. In the following, we use $\eta = 0.5$ and the parameters for the electromagnetic fields are the same as in the spinless case of § 3.1 (circularly polarized wave).

We will first compare the full models for short times (§ 3.2.1), then we consider a simplified model (neglecting self-consistency) for long times (§ 3.2.2), and finally we compare results for the full models at long times (§ 3.2.3).

3.2.1. *Full spin-dependent models at short times*

In this part, we focus on the solutions for short times (approximately $100\omega_p^{-1}$), which enables us to employ refined numerical parameters in order to compare as accurately as possible the two models.

From Proposition 1, we proved the equivalence between the scalar and vector models. However, this equivalence is only true for $\gamma \neq 0$, so that the term $\gamma \hbar \nabla (B \cdot \partial/\partial s) \cdot \partial f/\partial p$ is present in the scalar Vlasov equation (2.15). This term cannot be easily described using standard PIC methods based on trajectories, hence, it is neglected most of the time. However, when $\hbar = 0$ this term disappears, so that the two models are again equivalent for any value of γ. Then, by progressively increasing $\hbar$, we can show how the results of the scalar and vector models depart from each other. The numerical solutions are obtained using the PIC code described in our earlier work (Crouseilles *et al.* 2021) and the grid-based Eulerian code presented in the preceding section of the present paper.

To control the influence of the numerical error, we use a refined mesh for both methods: $N_x = 258$ and $N_p = 10^3$ for the grid-based method, and $N_x = 258$ with number of particles $N_{\mathrm{part}} = 10^5$ for the PIC method. The initial conditions are given by (3.10) with $\eta = 0.5$, $\alpha = 0.02$, $v_{\mathrm{th}} = 0.17$ and $E_0 = E_{\mathrm{ref}}$. Finally, the time step is $\Delta t = 0.004$ for both cases (both methods use a Strang splitting) and we consider the following values for the scaled Planck constant $\hbar = 0$, 0.001, 0.1, 0.25, 0.5, 0.75 and 1. We note that, strictly speaking, for such large values of $\hbar$ a relativistic treatment of the motion should be adopted. However, here the purpose is simply to study the agreement between the scalar and vector models, so that all considerations about relativistic corrections are ignored.

In figure 3, we study the difference ('error') between the scalar and vector models by considering the perpendicular electric energy $\mathcal{H}_{E,\perp} = \frac{1}{2} \int (E_y^2 + E_z^2) \, \mathrm{d}x$ and the magnetic energy $\mathcal{H}_B = \frac{1}{2} \int (B_y^2 + B_z^2) \, \mathrm{d}x$. We plot, on a log–log scale, the error (in the L^∞ norm) of these energies obtained from the scalar and vector models, for different values of $\hbar$. For both energies, the difference decreases with decreasing $\hbar$ in an approximately linear
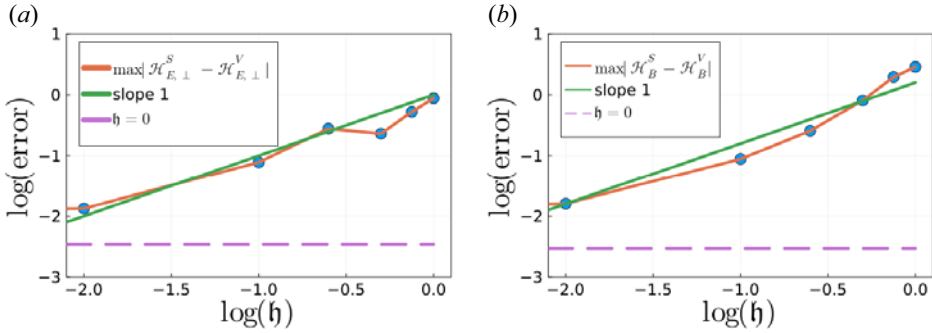
FIGURE 3. Difference (L^∞ norm) between the scalar (superscript S) and vector (superscript V) models for the perpendicular electric energy ($\mathcal{H}_{E,\perp}$, a) and magnetic energy ($\mathcal{H}_B$, b), for different values of the scaled Planck constant $\hbar$. The horizontal dashed lines correspond to the numerical error observed for $\hbar = 0$. The green straight line has a slope equal to unity.

fashion. This is in agreement with the fact that, for $\gamma = 0$, the difference between two models is expected to be $O(\hbar)$. For very small values of $\hbar$, the difference between the two models saturates to the numerical error due to the different numerical methods (PIC and Eulerian). The horizontal dashed line in figure 3 corresponds to such numerical error observed for $\hbar = 0$.

3.2.2. *Spin-dependent models without wave self-consistency at long times*

Here, we study the propagation of a circularly polarized wave into a plasma that does not retroact on the wave in the transverse direction, although the self-consistency along the propagation direction is maintained through the Poisson equation (Crouseilles *et al.* 2021). To simulate this, we consider a reduced model. Using the above notations, we remove the term $\frac{1}{2} \int_\Omega |\boldsymbol{A}_\perp|^2 f_0 \, dx \, dp$ from the Hamiltonian $\mathcal{H}$ in (2.21), then through the Poisson bracket representation (2.22) we can derive a reduce system similar to (2.19), but without the terms $\boldsymbol{A}_\perp \cdot (\partial \boldsymbol{A}_\perp/\partial x)(\partial f_0/\partial p)$ and $\boldsymbol{A}_\perp \cdot (\partial \boldsymbol{A}_\perp/\partial x)(\partial f/\partial p)$ in the Vlasov equations, and the terms $A_y \int_\mathbb{R} f_0 \, dp$ and $A_z \int_\mathbb{R} f_0 \, dp$ in the sources of the Maxwell equations. In this case, the electromagnetic wave is not coupled to the plasma and its evolution can be determined exactly by solving the corresponding Maxwell equations for E_y and E_z. In contrast, the longitudinal nonlinearity is kept in the model, hence, E_x is a solution of Poisson's equation.

We consider the initial condition (3.10) for the distribution functions and we use $\eta = 0.5$, $\alpha = 0.02$, $v_{\text{th}} = 0.17$ and $\hbar = 0.00022$. The electromagnetic fields are initialized as in the spinless case (see § 3.1), but here we have different matching conditions for the circularly polarized wave, since the wave propagates in vacuum in this case. We still have the relation (3.3a,b) together with the following ones:

$$\omega_{0,s} = k_{0,s}, \quad \omega_e^2 = 1 + 3k_e^2 v_{\text{th}}^2. \tag{3.11a,b}$$

We still consider $k_0 = 2k_e$, so that we obtain from the matching relations (3.3a,b) and (3.11a,b),

$$\omega_0 = 2.0928, \quad k_s = k_e = \omega_s = \omega_e = 1.0464. \tag{3.12a,b}$$

The amplitude of the incident wave is $E_0 = E_{\text{ref}} = 0.325$.

Neglecting the spatial dependence and considering the following time dependent magnetic field $\boldsymbol{B} = (0, B_0 \sin(\omega_0 t), -B_0 \cos(\omega_0 t))$ with $B_0 = E_0 k_0/\omega_0$, one can obtain an approximate closed equation for the dynamics of the macroscopic spin $S_z(t)$ (with $S_z(t) = \frac{1}{3} \int f_3 \, dx \, dp$ for the vector case and $S_z(t) = \int s_3 f \, dx \, dp \, ds$ for the scalar case). In

the regime $B_0/\omega_0 \ll 1$ (i.e. when the Larmor precession frequency eB_0/m is much smaller than the laser frequency), it can be shown that the spin $S_z(t)$ oscillates with a frequency $\omega_{\mathrm{spin}} = B_0^2/(2\omega_0)$ (see Crouseilles *et al.* (2021) for more details).

On the numerical side, we use the same parameters as in § 3.1 (i.e. $N_x = N_p = 129$ and $\Delta t = 0.04$) for the Eulerian method and $N_x = 128$, $N_{\mathrm{part}} = 2 \times 10^4$, $\Delta t = 0.04$ for the PIC method. Different values of the incident wave amplitude E_0 are studied to compare the numerical results with the analytic frequency $\omega_{\mathrm{spin}} = B_0^2/(2\omega_0)$. Indeed, as the transverse retroaction terms were removed from the Vlasov equation, we do not expect an instability here, so that the amplitude of the incident wave should remain approximately constant, which justifies the analytical calculations.

In figure 4, the time evolution of S_z obtained by the vector model (Eulerian method) and scalar model (PIC method) are displayed for three values of the amplitude of the incident electromagnetic wave E_0. The corresponding spectrum, normalized to its peak value, is also shown in figure 4(*b,d,f*). We observe that S_z displays an oscillatory damped behaviour for all cases, with a damping rate that is significantly higher when E_0 increases. The damping rate is slightly larger for the vector model at long times, but the agreement between the two approaches is very good for short times (up to $\approx 1500\omega_p^{-1}$). In the spectrum, the expected analytical frequencies $\omega_{\mathrm{spin}} = 0.0039$, 0.0158 and 0.063 are also recovered with good precision. In particular, the quadratic scaling between ω_{spin} and B_0 is correctly reproduced.

3.2.3. *Full spin-dependent models at long times*

Here, we present numerical results corresponding to $\alpha = 1$, $\beta = 1$, $\gamma = 0$ for the scalar and vector models for large times (the short time behaviour was investigated in § 3.2.1). In this case, the models are not equivalent as soon as $\hbar \neq 0$; however, the Poisson bracket structure is ensured for both models, so that the Hamiltonian splitting can be used (Strang splitting) to get a good total energy conservation for both codes. The initial condition for the distribution functions is that of (3.10) and the electromagnetic waves are circularly polarized, with the same parameters as in the spinless case of § 3.1.

Eulerian code results (vector model). First, we illustrate the general results obtained with the Eulerian (vector approach), before proceeding to the systematic comparison with the PIC code (scalar approach). The results, which were obtained with $\hbar = 0.00022$, are shown in figures 5 and 6.

The instability rate measured from the growth of the longitudinal electric field amplitude $\|E_x(t)\|$ is close to the one observed in the spinless simulations ($\gamma_{\mathrm{inst}} \approx 0.03$). Moreover, the magnetic field energy strongly decreases during the linear phase (where the longitudinal electric energy increases exponentially) to reach a plateau, before another strong drop around $t \approx 2000\omega_p^{-1}$. Finally, the spin component $S_z(t) = \frac{1}{3}\int f_3\,\mathrm{d}x\,\mathrm{d}p$ has a damped oscillatory behaviour which is qualitatively similar to the results obtained with the PIC approach (Crouseilles *et al.* 2021).

We also show, in figure 6, the phase space portraits of the distribution functions f_0, f_1, f_2, f_3 at time $t = 320\omega_p^{-1}$. Two phase-space vortices can be clearly seen in these figures thanks to the high-order numerical methods used for these Eulerian simulations. As expected, the size of each vortex is close to the wavelength of the unstable plasma wave $2\pi/k_e \approx 5.15$ (see § 3.1). We note that the statistical noise inherent to PIC codes would have precluded such high-resolution diagnostics.

Comparison with PIC code (scalar model) for $\hbar = 0$. In figure 7, we compare the vector and scalar models with $E_0 = 2E_{\mathrm{ref}}$ and $\hbar = 0$. When $\hbar = 0$ and $\alpha = \beta = 1$, $\gamma = 0$, the scalar and vector models are mathematically equivalent, but the results may differ because
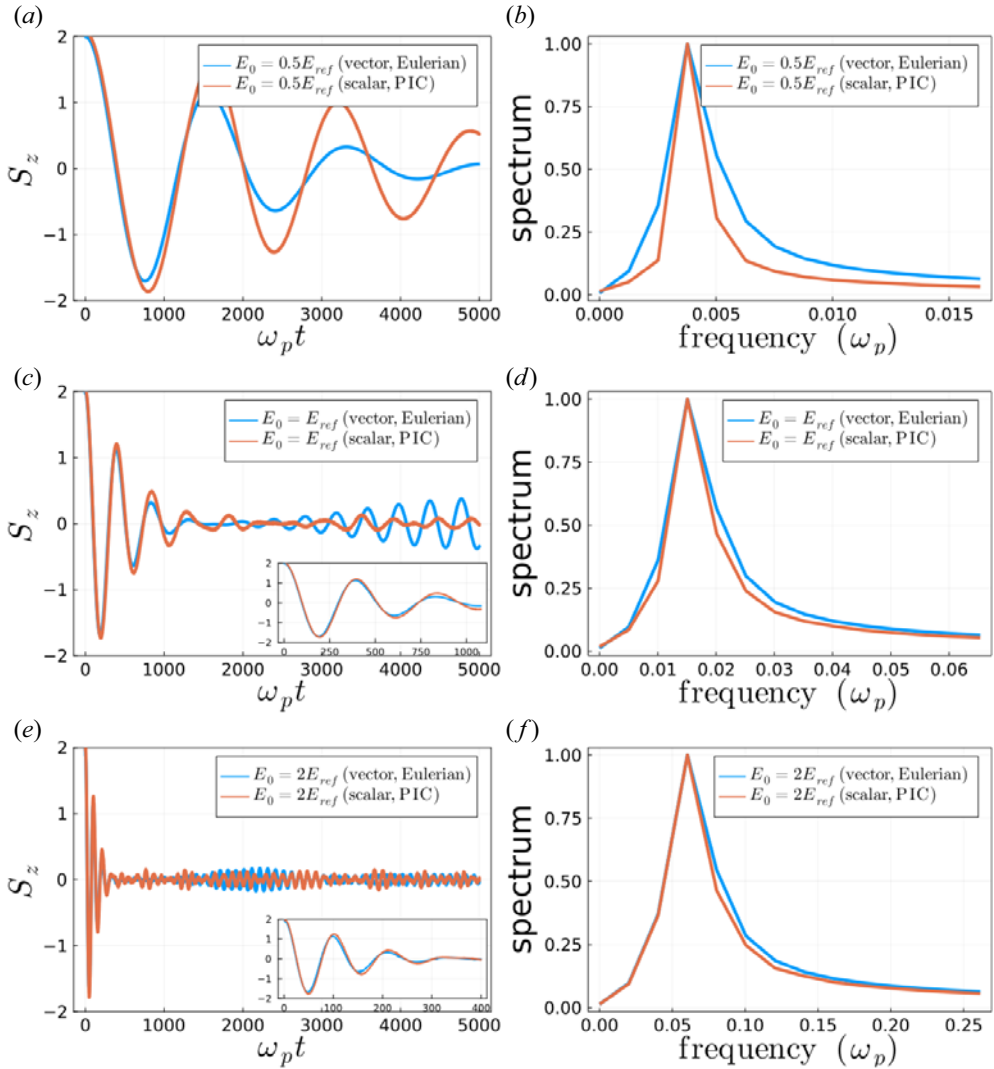
FIGURE 4. Spin-dependent reduced model without wave self-consistency. Time evolution of S_z (a,c,e) and frequency spectrum of S_z (b,d,f), for the scalar (red lines) and vector (blue lines) models. We recall that $S_z = \int s_3 f \, dx \, dp \, ds$ for the vector model (Eulerian code) and $S_z = \frac{1}{3} \int f_3 \, dx \, dp$ for the scalar model (PIC code). The amplitude of the incident wave is, from top to bottom, $E_0 = 0.5 E_{\text{ref}}$, $E_0 = E_{\text{ref}}$ and $E_0 = 2 E_{\text{ref}}$. The analytical predictions for the peak frequency are $\omega_{\text{spin}} = 0.0039$, 0.0158 and 0.063, from top to bottom.

of the different numerical methods that are used. Therefore, this is a good comparative test of the two numerical methods.

First, we observe that the instability rate on $\|E_x(t)\|$ is similar for the two approaches, and very close to the one observed in the spinless case ($\gamma_{\text{inst}} \approx 0.06$). We also checked that the growth rate is linear with respect to E_0 by running the case $E_0 = E_{\text{ref}}$ (twice as small as in figure 7) and that the total energy is very well conserved (with an error $\approx 10^{-5}$ even for long times, for both codes). Second, we can see that the spin frequencies obtained from the PIC and Eulerian simulations are very similar ($\approx 0.08 \omega_p$).
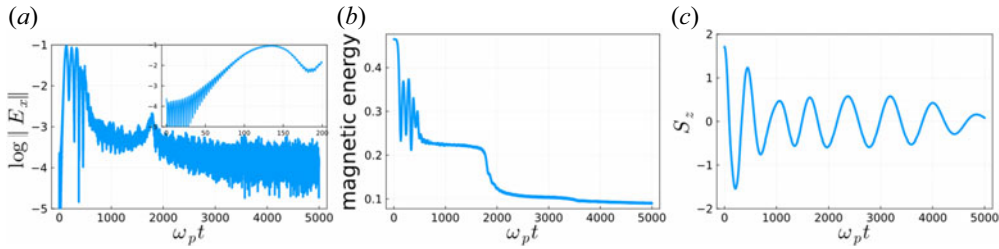
FIGURE 5. Full spin-dependent vector model (Eulerian method with $N_x = 259$, $N_p = 512$, $p \in [-2.5, 2.5]$, $\Delta t = 0.02$). (*a*) Longitudinal electric field norm $\|E_x\|$ in semilog scale (the inset shows a zoom on short times to highlight the linear instability phase with slope ≈ 0.03). (*b*) Magnetic energy $\frac{1}{2} \int |\boldsymbol{B}|^2 \, dx$. (*c*) Spin component $S_z(t)$.

Generally speaking, the results of the two codes are in good agreement, particularly during the initial linear phase. The remaining observed differences should be attributed to the two numerical methods (PIC and Eulerian), which are intrinsically different in their approaches.

Effect of the scaled Planck constant. In figures 8, 9 and 10, the influence of $\hbar$ ($\hbar = 0.01$, 0.1 and 0.5) is studied for the vector and scalar models for $E_0 = 2E_{\text{ref}}$. The same initial condition as before is used and $\alpha = \beta = 1$, $\gamma = 0$. Let us recall that here, since $\hbar \neq 0$, the two models are not mathematically equivalent. The linear phase becomes quite different as $\hbar$ increases: in particular, the electric energies do not saturate at the same level. However, the evolution of S_z is similar for both approaches: the oscillations are damped more quickly as $\hbar$ increases. For both codes, the total energy is well preserved (the relative error is approximately 10^{-4}, not shown). Finally, the magnetic energies, even though they both decrease in the two approaches, have rather different behaviours, with a bigger drop observed for the vector model. Of course, the differences can be explained by the fact that in this case the underlying models are not equivalent. We emphasize that the Eulerian code has been tested on several meshes to ensure the numerical convergence, whereas the PIC code would require, in order to achieve convergence, a large number of particles N_p that would lead to very time-consuming simulations.

Finally, we note, by comparing figures 8(*e*,*f*), 9(*e*,*f*) and 10(*e*,*f*), that the spin oscillations are more strongly damped for larger values of $\hbar$.

Temperature effects. In figure 11, we study the influence of a higher electron temperature by taking $v_{\text{th}} = 0.51$ in the initial condition (3.10) for the Eulerian and PIC codes (instead of $v_{\text{th}} = 0.17$ in figure 5). The field amplitude is fixed to $E_0 = E_{\text{ref}}$ and $\hbar = 0.00022$. For the present case $v_{\text{th}} = 0.51$, the matching relations (3.3*a*,*b*) and (3.4*a*,*b*) yield the wavenumbers $k_e = 1.46$ and $k_0 = 2k_e$. In figure 11, we show the time evolution of the electric energy and the spin component S_z for the Eulerian and PIC methods. These results have to be compared with the case $v_{\text{th}} = 0.17$ presented in figure 5.

Thanks to its superior resolution, the Eulerian code allows the initial longitudinal electric field to be very small (figure 11*a*), in accordance with the initial condition (3.10). Subsequently, this initial perturbation grows unstable and saturates nonlinearly at a certain (still rather small) value. The spikes observed on the figure correspond to the well-known recurrences occurring at times multiple of $2\pi/(k_e \Delta p)$, where Δp is the grid step in momentum space. These recurrences are due to the discretization of momentum space. In contrast, the PIC code (figure 11*b*) cannot resolve the initial small perturbation because of its inherent noise, so the instability is lost. Indeed, the noise level of the PIC code is even higher than the saturation level observed for the Eulerian code.
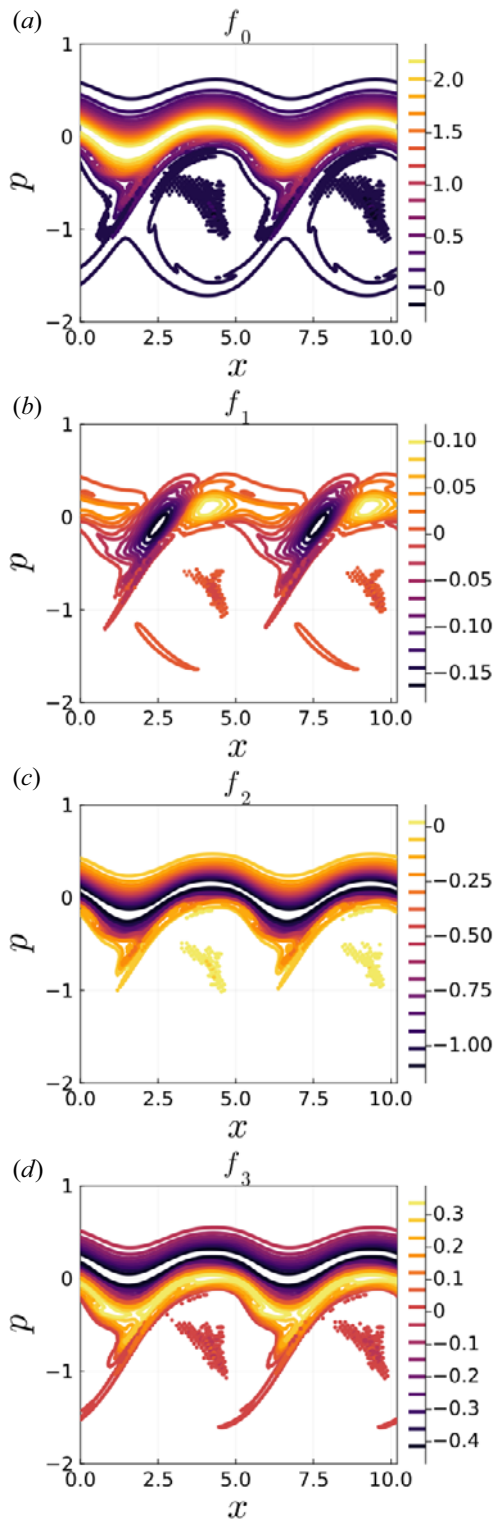
FIGURE 6. Full spin-dependent vector model (Eulerian method with $N_x = 129$, $N_p = 256$, $p \in [-2.5, 2.5]$, $\Delta t = 0.04$). From (a) to (d): contour plots of the four components of the electron distribution function f_0, f_1, f_2, f_3 in the phase space (x, p), at time $t = 320\omega_p^{-1}$.
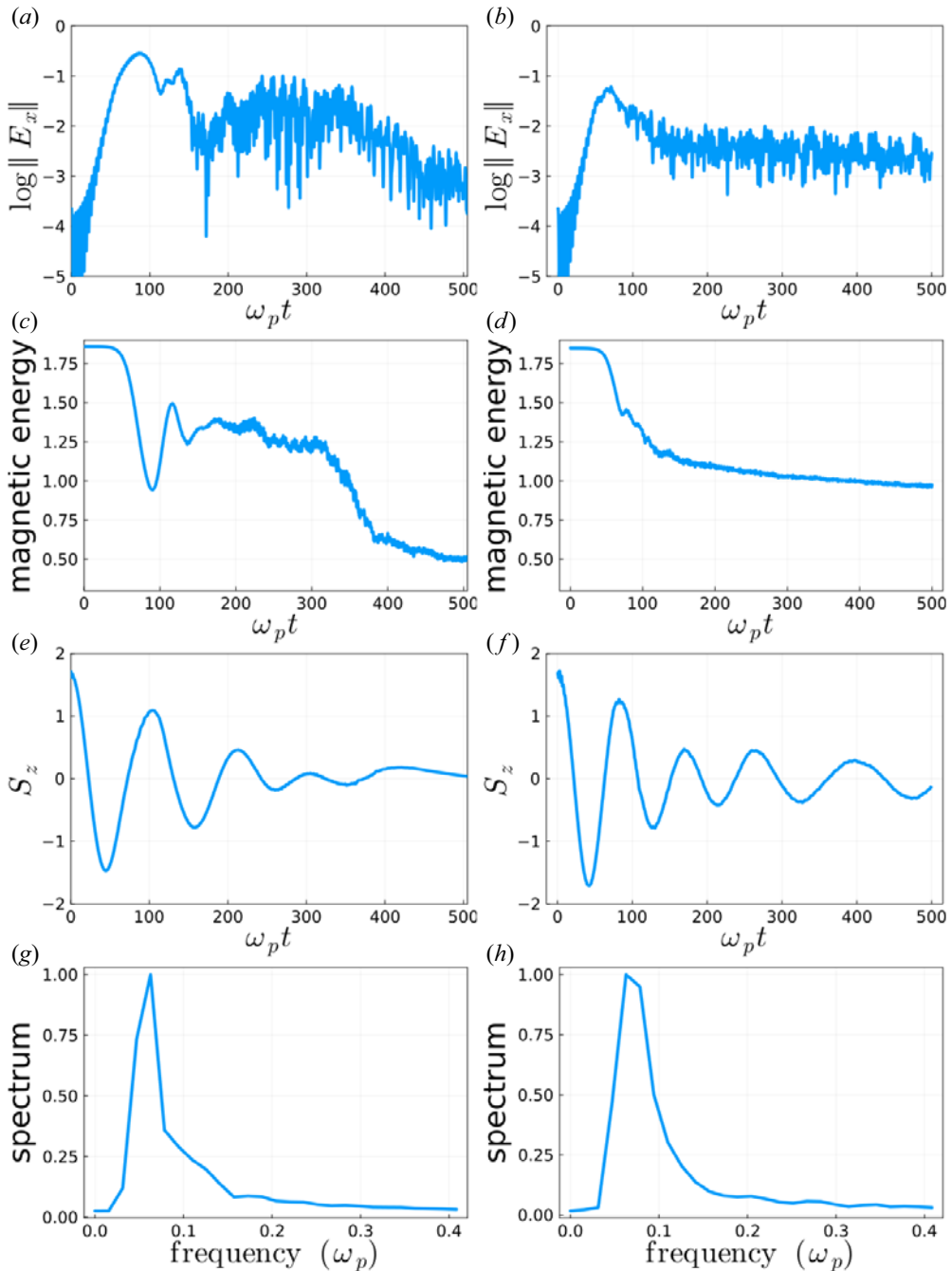
FIGURE 7. Comparison of the full spin-dependent vector and scalar models with $\hbar = 0.0$ and $E_0 = 2E_{\text{ref}}$ (Eulerian method with $p \in [-5, 5]$ $N_x = 259$, $N_p = 512$, $\Delta t = 0.02$ and PIC method with $N_x = 259$, $N_{\text{part}} = 10^5$, $\Delta t = 0.02$). (*a,c,e,g*) Vector model with Eulerian method; (*b,d,f,h*) scalar model with PIC method. From top to bottom are shown (*a,b*) the longitudinal electric field, (*c,d*) the magnetic energy, (*e,f*) the spin component S_z, and (*g,h*) its frequency spectrum.
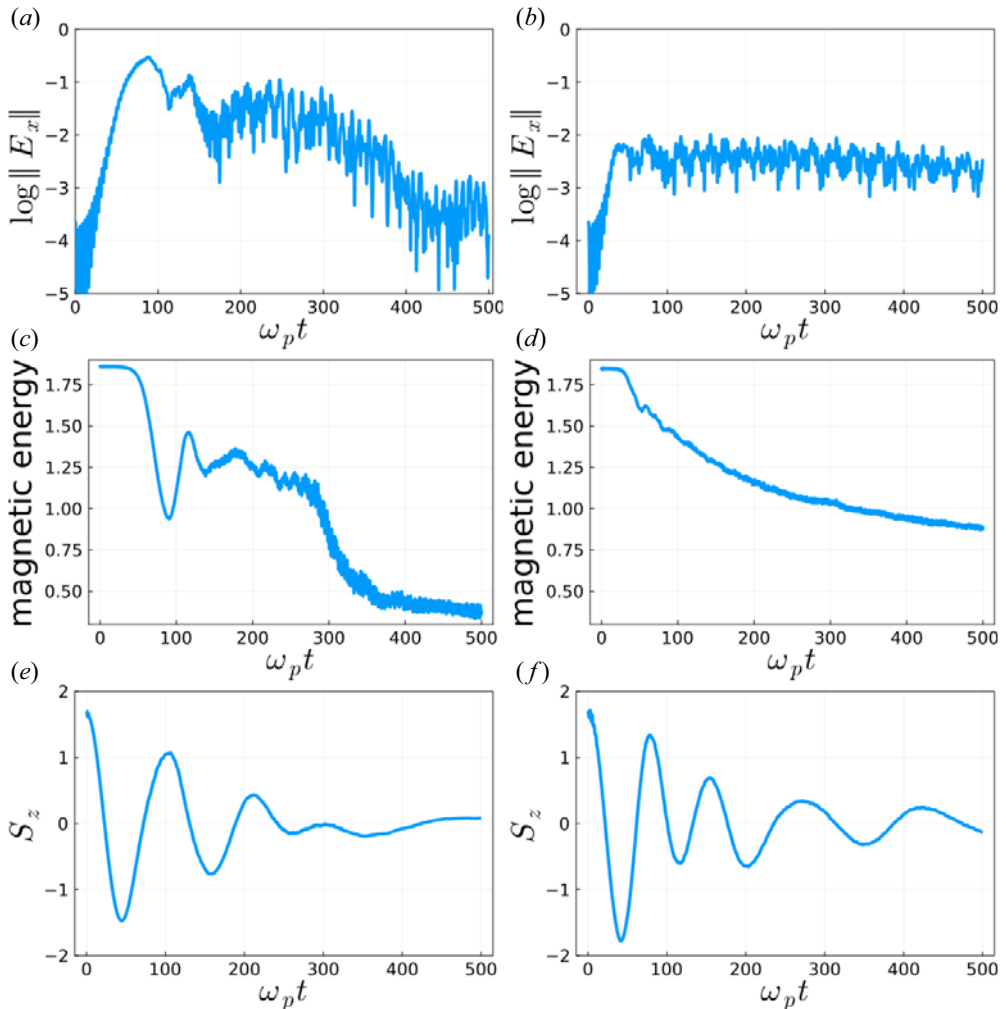
FIGURE 8. Comparison of the full spin-dependent vector and scalar models for $\mathfrak{h} = 0.01$ and $E_0 = 2E_{\text{ref}}$ (Eulerian method with $p \in [-5, 5]$ $N_x = 259$, $N_p = 512$, $\Delta t = 0.02$ and PIC method with $N_x = 259$, $N_{\text{part}} = 10^5$, $\Delta t = 0.02$). (a,c,e) Vector model with Eulerian method; (b,d,f) scalar model with PIC method. From top to bottom, we show (a,b) the time evolution of the longitudinal electric field, (c,d) the magnetic energy, and (e,f) the spin component S_z.

In spite of these limitations, the spin component S_z decreases in a similar fashion for both methods, and becomes almost zero after $\omega_p t = 1000$.

By comparing the results of figure 11 ($v_{\text{th}} = 0.17$) and figure 5 ($v_{\text{th}} = 0.51$), we also note that the spin component S_z is more strongly damped for the case at higher temperature, as should be expected.

Full vector model with $\gamma \neq 0$. In this last part, we simulate the full spin-Vlasov–Maxwell vector model introduced in Hurst *et al.* (2014, 2017) and Manfredi *et al.* (2022), i.e. for $\gamma = 1, \alpha = 3, \beta = 1$, for which we cannot perform simulations for the scalar model, since the cross-derivative term is not implemented in our PIC code. In particular, we compare the results of the Eulerian code for this set of parameters (with $\gamma \neq 0$) with those obtained with the same code but $\gamma = 0$ and $\alpha = \beta = 1$ (see figure 9).
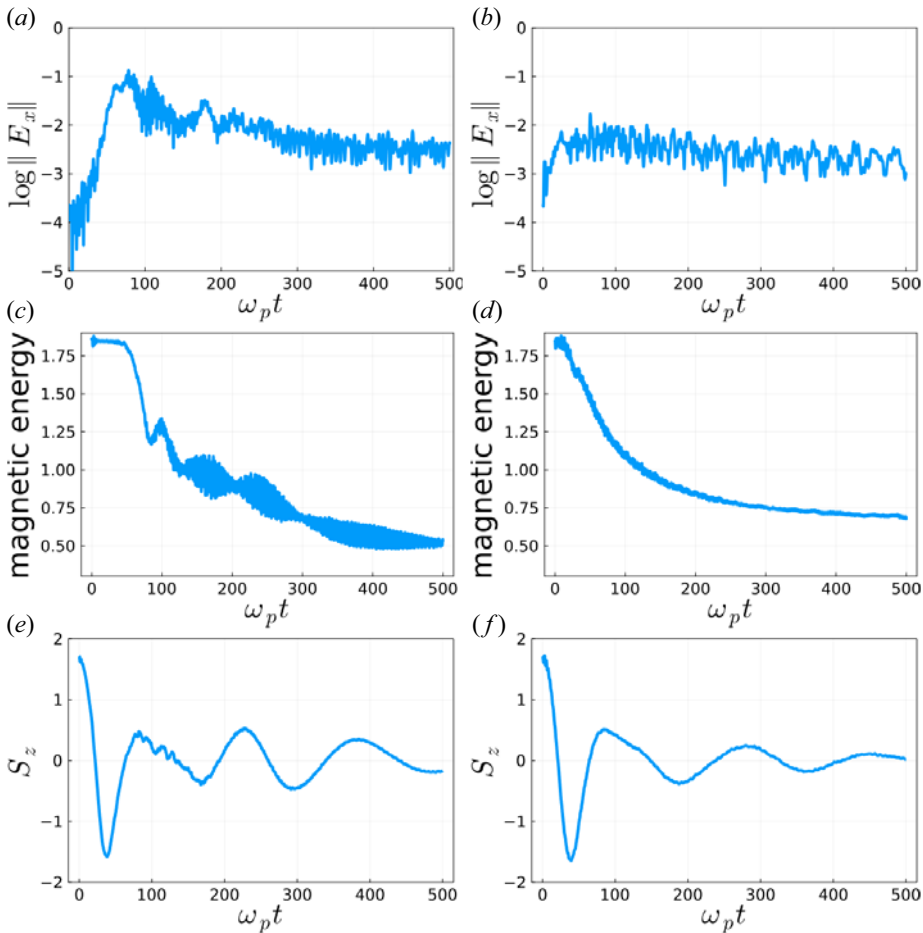
FIGURE 9. Same as figure 8 for $\mathfrak{h} = 0.1$.

In figure 12, we show the comparison for a typical case with $E_0 = 2E_{\text{ref}}$ and $\mathfrak{h} = 0.1$. The results are in reasonable agreement: in particular, the longitudinal electric fields and the magnetic energies saturate nonlinearly at similar levels. The z component of the spin appears to decay faster and with fewer oscillations in the $\gamma \neq 0$ case. For both cases, the total energy is very well preserved (around 10^{-4}, not shown).

4. Conclusion

Here, we implemented and analysed the results of an Eulerian code that solves the self-consistent Vlasov–Maxwell equations for particles with spin 1/2. In this case, the phase-space distribution function has actually four components, which can be rearranged as one scalar and one vector distribution. This model was termed 'vectorial model' in the present work. We also compared the results with those obtained (using a PIC code) with a fully scalar model in an extended phase space that includes the spin variable – see our recent work (Crouseilles *et al.* 2021).

In order to make systematic comparisons, we appended some artificial coefficients, α, β and γ to the equations, and checked the equivalence between the scalar and vector models. In particular, the scalar model includes a peculiar term that contains a double derivative
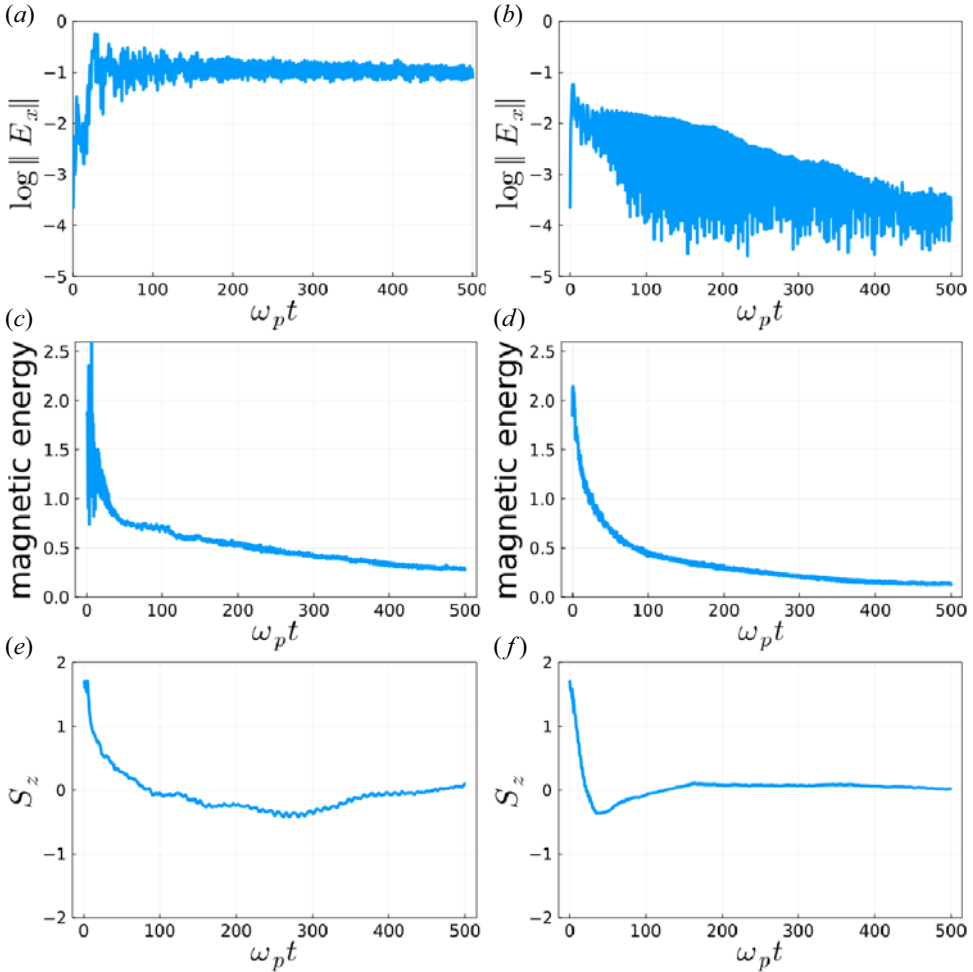
FIGURE 10. Same as figure 8 for $\mathfrak{h} = 0.5$.

in the momentum and spin variables. Due to this term, it is impossible to write the Vlasov equation in characteristic form, and, hence, to use a standard PIC code base on particle trajectories. Therefore, this term was neglected in earlier simulations (Crouseilles *et al.* 2021), which amounts to taking $\gamma = 0$ in our notation. However, we stress that this is a quantum term, and its absence may bring into question the fully quantum nature of the scalar model, see Zamanian *et al.* (2010) for a discussion on this point.

A second issue is the existence of a Poisson structure, which is important to construct efficient numerical methods that preserve the Hamiltonian structure of the equations (Kraus *et al.* 2017) and, hence, avoid numerical dissipation. For the scalar model with $\gamma = 0$, a non-canonical Poisson structure exists when $\alpha = \beta$, which was used in our earlier work using a PIC code (Crouseilles *et al.* 2021). For the vector model, the structure exists when $\alpha = \beta + 2\gamma$, which reduces to the same relationship as for the scalar model when $\gamma = 0$.

Therefore, we compared systematically the two approaches in the case $\alpha = \beta = 1$ and $\gamma = 0$, for a standard plasma problem, namely the Raman instability. However, it must be stressed that the two models are not mathematically equivalent in this
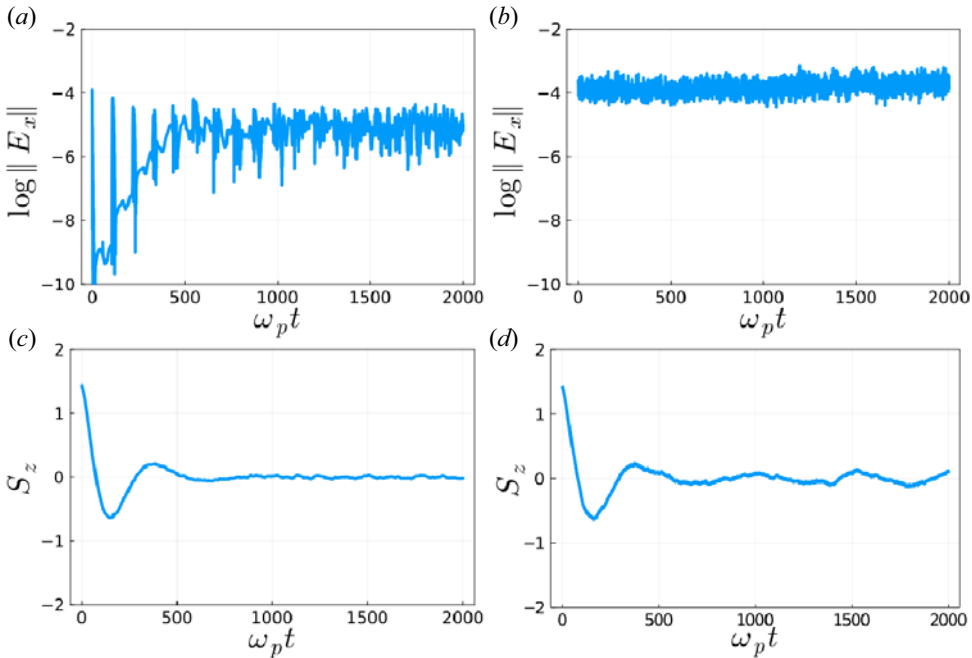
FIGURE 11. Influence of the electron temperature using $v_{th} = 0.51$. (*a,b*) Time evolution of the electric energy (semilog scale). (*c,d*) Time evolution of the spin S_z. (*a,c*) Full spin-dependent vector model (Eulerian method with $N_x = N_p = 129$, $\Delta t = 0.04$). (*b,d*) Full spin-dependent scalar model (PIC method with $N_x = 129$, $N_{part} = 2 \times 10^4$, $\Delta t = 0.04$).

case, so that the observed discrepancies may come from either the models themselves or from the different numerical methods. Moreover, in the classical limit $\hbar = 0$, the scalar and vector models are again equivalent (because the double-derivative term is a quantum one, as pointed out above), so in this case a meaningful test of the two codes was possible. The results were encouraging, particularly on the initial linear phase of the Raman instability and on the damping of the spin amplitude. Comparisons for $\hbar > 0$ also showed a reasonable accordance between the two approaches, and revealed that the discrepancies progressively disappear with decreasing scaled Planck constant, as expected.

For the full model ($\gamma = 1$) it is not possible to use the PIC code because of the double derivative problem. Hence, we compared results obtained with the vector model and the Eulerian code for the cases $\gamma = 0$ and $\gamma = 1$. Even though the behaviour is similar, we observed that the spin is damped faster in the case $\gamma = 1$.

In summary, the Eulerian code described here is able to simulate the quantum dynamics of a spin polarized electron plasma. Contrarily to the scalar model, no simplifications need to be made to implement the corresponding numerical code. Hence, the dynamics is fully quantum, at least for the spin variable, whereas, as usual, the orbital motion is treated classically. In addition, the well-known high-resolution properties of grid-based Eulerian codes outperform their PIC counterparts in many respects, particularly for subtle effects that occur at low particle density, such as the formation of phase-space vortices. The present Eulerian code is thus a valuable tool for further studies in this domain.
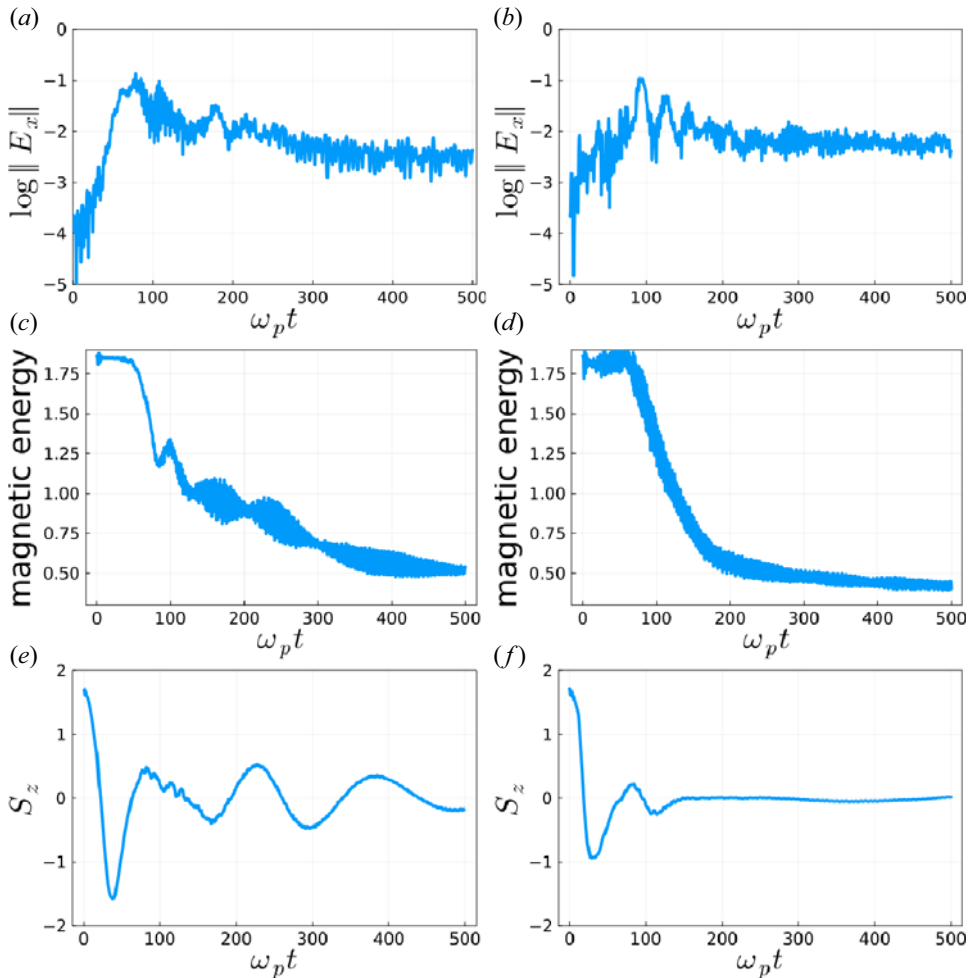
FIGURE 12. Eulerian method for the vector model with $\alpha = \beta = 1, \gamma = 0$ (a,c,e) and $\alpha = 3, \beta = \gamma = 1$ (b,d,f) with $\mathfrak{h} = 0.1$. $N_x = 259, N_p = 10^3, \ \Delta t = 0.02, E_0 = 2E_{\mathrm{ref}}$. From top to bottom, we show (a,b) the norm of the longitudinal electric field, (c,d) the magnetic energy, and (e,f) the z component of the spin.

Declaration of interests

The authors report no conflict of interest.

Appendix A. Proof of Proposition 1

First of all, we give some calculations concerning the spherical coordinates transformation,

$$
\left.
\begin{aligned}
\partial_{s_i} s_j = -s_i s_j, \quad i,j = 1,2,3 \; i \neq j, \text{ and } \partial_{s_i} s_i = 1 - s_i^2 \\[4pt]
\partial_{s_1} s_1 = \frac{s_1^2 s_3^2 + s_2^2}{s_1^2 + s_2^2} = 1 - s_1^2, \\[4pt]
\partial_{s_2} s_2 = \frac{s_2^2 s_3^2 + s_1^2}{s_1^2 + s_2^2} = 1 - s_2^2, \\[4pt]
\partial_{s_3} s_3 = s_1^2 + s_2^2 = 1 - s_3^2.
\end{aligned}
\right\}
\tag{A1}
$$

Now, assuming that the initial condition satisfies $f(t=0) = (1/4\pi)(f_0(t=0) + \boldsymbol{s} \cdot \boldsymbol{f}(t=0))$, we check that $f(t) = (1/4\pi)(f_0(t) + \boldsymbol{s} \cdot \boldsymbol{f}(t)) = (1/4\pi)(f_0(t) + \sum_i s_i f_i(t))$ is true for all times $t > 0$. To do so, we insert the decomposition $f(t) = (1/4\pi)(f_0(t) + \boldsymbol{s} \cdot \boldsymbol{f}(t))$ into the scalar equation (2.2). Of course, the terms $\partial f/\partial t$, $\boldsymbol{p} \cdot \boldsymbol{\nabla} f$ and $[\boldsymbol{E} + \boldsymbol{p} \times \boldsymbol{B}] \cdot \partial f/\partial \boldsymbol{p}$ satisfy this property. Let us focus on the other terms $(\boldsymbol{s} \times \boldsymbol{B}) \cdot \partial f/\partial \boldsymbol{s}$, $\hbar \boldsymbol{\nabla}(\boldsymbol{s} \cdot \boldsymbol{B}) \cdot \partial f/\partial \boldsymbol{p}$ and $\hbar \boldsymbol{\nabla}(\boldsymbol{B} \cdot \partial/\partial \boldsymbol{s}) \cdot \partial f/\partial \boldsymbol{p}$ by using the relations (A1).

For the first term, we have

$$
\begin{aligned}
(\boldsymbol{s} \times \boldsymbol{B}) \cdot \frac{\partial f}{\partial \boldsymbol{s}} &= \frac{1}{4\pi}(\boldsymbol{s} \times \boldsymbol{B}) \cdot \frac{\partial(f_0 + \boldsymbol{s} \cdot \boldsymbol{f})}{\partial \boldsymbol{s}} = \frac{1}{4\pi}(\boldsymbol{s} \times \boldsymbol{B}) \cdot \frac{\partial(\boldsymbol{s} \cdot \boldsymbol{f})}{\partial \boldsymbol{s}} \\[6pt]
&= \frac{1}{4\pi}\left(\frac{\partial(\boldsymbol{s} \cdot \boldsymbol{f})}{\partial \boldsymbol{s}} \times \boldsymbol{s}\right) \cdot \boldsymbol{B} \\[6pt]
&= \frac{1}{4\pi}\left(\sum_{j=1}^{3} f_j \frac{\partial s_j}{\partial \boldsymbol{s}} \times \boldsymbol{s}\right) \cdot \boldsymbol{B} = \frac{1}{4\pi}(\boldsymbol{f} \times \boldsymbol{s}) \cdot \boldsymbol{B} = \frac{1}{4\pi} \boldsymbol{s} \cdot (\boldsymbol{B} \times \boldsymbol{f}).
\end{aligned}
\tag{A2}
$$

Regarding the second term $\beta \hbar \boldsymbol{\nabla}(\boldsymbol{s} \cdot \boldsymbol{B}) \cdot \partial f/\partial \boldsymbol{p}$, we have

$$
\begin{aligned}
\hbar \boldsymbol{\nabla}(\boldsymbol{s} \cdot \boldsymbol{B}) \cdot \frac{\partial f}{\partial \boldsymbol{p}} &= \frac{\hbar}{4\pi} \boldsymbol{\nabla}(\boldsymbol{s} \cdot \boldsymbol{B}) \cdot \frac{\partial(f_0 + \boldsymbol{s} \cdot \boldsymbol{f})}{\partial \boldsymbol{p}} \\[6pt]
&= \frac{\hbar}{4\pi} \boldsymbol{\nabla}(\boldsymbol{s} \cdot \boldsymbol{B}) \cdot \frac{\partial f_0}{\partial \boldsymbol{p}} + \frac{\hbar}{4\pi} \boldsymbol{\nabla}(\boldsymbol{s} \cdot \boldsymbol{B}) \cdot \frac{\partial(\boldsymbol{s} \cdot \boldsymbol{f})}{\partial \boldsymbol{p}} \\[6pt]
&= \frac{\hbar}{4\pi} \boldsymbol{\nabla}(\boldsymbol{s} \cdot \boldsymbol{B}) \cdot \frac{\partial f_0}{\partial \boldsymbol{p}} + \frac{\hbar}{4\pi} \sum_{i,j} s_i s_j (\boldsymbol{\nabla} B_i) \cdot \frac{\partial f_j}{\partial \boldsymbol{p}} \\[6pt]
&= \frac{\hbar}{4\pi} \boldsymbol{\nabla}(\boldsymbol{s} \cdot \boldsymbol{B}) \cdot \frac{\partial f_0}{\partial \boldsymbol{p}} + \frac{\hbar}{4\pi} \sum_{i \neq j} s_i s_j (\boldsymbol{\nabla} B_i) \cdot \frac{\partial f_j}{\partial \boldsymbol{p}} + \frac{\hbar}{4\pi} \sum_i s_i^2 (\boldsymbol{\nabla} B_i) \cdot \frac{\partial f_i}{\partial \boldsymbol{p}} \\[6pt]
&= \frac{\hbar}{4\pi}\left[\sum_i s_i (\boldsymbol{\nabla} B_i) \cdot \frac{\partial f_0}{\partial \boldsymbol{p}} + \sum_{i \neq j} s_i s_j (\boldsymbol{\nabla} B_i) \cdot \frac{\partial f_j}{\partial \boldsymbol{p}} + \sum_i s_i^2 (\boldsymbol{\nabla} B_i) \cdot \frac{\partial f_i}{\partial \boldsymbol{p}}\right].
\end{aligned}
\tag{A3}
$$

Finally, the third term $\gamma \hbar \boldsymbol{\nabla}(\boldsymbol{B} \cdot \partial/\partial \boldsymbol{s}) \cdot \partial f/\partial \boldsymbol{p}$ becomes

$$
\hbar \boldsymbol{\nabla}\left(\boldsymbol{B} \cdot \frac{\partial}{\partial \boldsymbol{s}}\right) \cdot \frac{\partial f}{\partial \boldsymbol{p}} = \frac{\hbar}{4\pi} \boldsymbol{\nabla}\left(\boldsymbol{B} \cdot \frac{\partial}{\partial \boldsymbol{s}}\right) \cdot \frac{\partial(f_0 + \boldsymbol{s} \cdot \boldsymbol{f})}{\partial \boldsymbol{p}}
$$

$$
= \frac{\hbar}{4\pi} \nabla \left(\boldsymbol{B} \cdot \frac{\partial}{\partial \boldsymbol{s}} \right) \cdot \frac{\partial f_0}{\partial \boldsymbol{p}} + \frac{\hbar}{4\pi} \nabla \left(\boldsymbol{B} \cdot \frac{\partial}{\partial \boldsymbol{s}} \right) \cdot \frac{\partial (\boldsymbol{s} \cdot \boldsymbol{f})}{\partial \boldsymbol{p}}
$$

$$
= \frac{\hbar}{4\pi} \sum_{i,j} (\nabla B_i) \cdot \frac{\partial f_j}{\partial \boldsymbol{p}} \left(\frac{\partial}{\partial s_i} s_j \right)
$$

$$
= \frac{\hbar}{4\pi} \left[\sum_{i \neq j} (-s_i s_j)(\nabla B_i) \cdot \frac{\partial f_j}{\partial \boldsymbol{p}} + \sum_i (1 - s_i^2)(\nabla B_i) \cdot \frac{\partial f_i}{\partial \boldsymbol{p}} \right]
$$

$$
= \frac{\hbar}{4\pi} \left[-\sum_{i \neq j} s_i s_j (\nabla B_i) \cdot \frac{\partial f_j}{\partial \boldsymbol{p}} + \sum_i (\nabla B_i) \cdot \frac{\partial f_i}{\partial \boldsymbol{p}} - \sum_i s_i^2 (\nabla B_i) \cdot \frac{\partial f_i}{\partial \boldsymbol{p}} \right].
\tag{A4}
$$

Then, adding the contributions of these last three terms, we observe that the quadratic terms cancel out for $\beta = \gamma$ and we finally get for this case

$$
(\boldsymbol{s} \times \boldsymbol{B}) \cdot \frac{\partial f}{\partial \boldsymbol{s}} + \beta \hbar \nabla (\boldsymbol{s} \cdot \boldsymbol{B}) \cdot \frac{\partial f}{\partial \boldsymbol{p}} + \beta \hbar \nabla \left(\boldsymbol{B} \cdot \frac{\partial}{\partial \boldsymbol{s}} \right) \cdot \frac{\partial f}{\partial \boldsymbol{p}}
$$

$$
= \frac{1}{4\pi} \left[\sum_i s_i (\boldsymbol{B} \times \boldsymbol{f})_i + \beta \hbar \sum_i s_i (\nabla B_i) \cdot \frac{\partial f_0}{\partial \boldsymbol{p}} + \beta \hbar \sum_i (\nabla B_i) \cdot \frac{\partial f_j}{\partial \boldsymbol{p}} \right].
\tag{A5}
$$

Gathering all the terms of the scalar equation enables us to get

$$
0 = \frac{1}{4\pi} \frac{\partial (f_0 + \boldsymbol{s} \cdot \boldsymbol{f})}{\partial t} + \frac{1}{4\pi} \boldsymbol{p} \cdot \nabla (f_0 + \boldsymbol{s} \cdot \boldsymbol{f}) + \frac{1}{4\pi} (\boldsymbol{s} \times \boldsymbol{B}) \cdot \frac{\partial (f_0 + \boldsymbol{s} \cdot \boldsymbol{f})}{\partial \boldsymbol{s}}
$$

$$
+ \frac{1}{4\pi} \left[(\boldsymbol{E} + \boldsymbol{p} \times \boldsymbol{B}) + \beta \hbar \nabla (\boldsymbol{s} \cdot \boldsymbol{B}) + \beta \hbar \nabla \left(\boldsymbol{B} \cdot \frac{\partial}{\partial \boldsymbol{s}} \right) \right] \cdot \frac{\partial (f_0 + \boldsymbol{s} \cdot \boldsymbol{f})}{\partial \boldsymbol{p}}
$$

$$
= \frac{1}{4\pi} \left(\frac{\partial f_0}{\partial t} + \boldsymbol{p} \cdot \nabla f_0 + (\boldsymbol{E} + \boldsymbol{p} \times \boldsymbol{B}) \cdot \frac{\partial f_0}{\partial \boldsymbol{p}} + \beta \hbar \sum_i \nabla B_i \cdot \frac{\partial f_i}{\partial \boldsymbol{p}} \right)
$$

$$
+ \frac{1}{4\pi} \sum_i s_i \left(\frac{\partial f_i}{\partial t} + \boldsymbol{p} \cdot \nabla f_i + (\boldsymbol{E} + \boldsymbol{p} \times \boldsymbol{B}) \cdot \frac{\partial f_i}{\partial \boldsymbol{p}} + (\boldsymbol{B} \times \boldsymbol{f})_i + \beta \hbar \nabla B_i \cdot \frac{\partial f_0}{\partial \boldsymbol{p}} \right). \tag{A6}
$$

Since $(1, s_1, s_2, s_3)$ is a basis, we can identify the coefficients to be zero, which leads to the four equations of the vector model satisfied by (f_0, f_1, f_2, f_3). Thus, since f and $(1/4\pi)(f_0 + \boldsymbol{s} \cdot \boldsymbol{f})$ share the same initial condition, we get that $f = (1/4\pi)(f_0 + \boldsymbol{s} \cdot \boldsymbol{f})$ is a solution of the scalar model if and only if (f_0, f_1, f_2, f_3) is the solution of vector model (2.8).

Appendix B. Derivation of the 1-D vector model (Proposition 2)

To derive the vector model from the scalar one in the laser–plasma context considered in the main text, we will take the moments with respect to the variable $\boldsymbol{s}$ of the scalar model (2.15). Thus, we first multiply (2.15) by $(1, 3\boldsymbol{s})$, thus integrate with respect to $\boldsymbol{s}$ and finally,

use the representation

$$f(t, x, p, s) = \frac{1}{4\pi}(f_0(t, x, p) + s \cdot f(t, x, p)). \tag{B1}$$

We shall use the following identities which can be calculated from the spherical coordinates transformation using (B1):

$$\left. \begin{aligned}
\int f \, ds = f_0, \quad & \int s f \, ds = \frac{1}{3} f, \\
\int \frac{\partial f}{\partial s_i} \, ds = \frac{2}{3} f_i, \quad & \int s_i \frac{\partial f}{\partial s_j} \, ds = 0, \\
\int s_i^2 \frac{\partial f}{\partial s_i} \, ds = \frac{2}{15} f_i, \quad & \int s_i^2 \frac{\partial f}{\partial s_j} \, ds = \frac{4}{15} f_j, \\
\int s_i s_j \frac{\partial f}{\partial s_k} \, ds = 0, \quad & \int s_i s_j \frac{\partial f}{\partial s_i} \, ds = -\frac{1}{15} f_j.
\end{aligned} \right\} \tag{B2}$$

We integrate the first equation in (2.15) with respect to s on $\mathbb{S}^2$ and use (B1) and (B2) to get the following equation on f_0:

$$\frac{\partial f_0}{\partial t} + p \frac{\partial f_0}{\partial x} + \left(E_x - A_\perp \cdot \frac{\partial A_\perp}{\partial x} \right) \frac{\partial f_0}{\partial p} - \frac{(\beta + 2\gamma)}{3} \hbar \frac{\partial^2 A_z}{\partial x^2} \frac{\partial f_2}{\partial p} + \frac{(\beta + 2\gamma)}{3} \hbar \frac{\partial^2 A_y}{\partial x^2} \frac{\partial f_3}{\partial p} = 0. \tag{B3}$$

With our magnetic field ($B = (0, -\partial_x A_z, \partial_x A_y)$), this equation can be reformulated as

$$\frac{\partial f_0}{\partial t} + p \frac{\partial f_0}{\partial x} + \left(E_x - A_\perp \cdot \frac{\partial A_\perp}{\partial x} \right) \frac{\partial f_0}{\partial p} + \frac{(\beta + 2\gamma)}{3} \hbar \sum_{j=1}^{3} \frac{\partial B_j}{\partial x} \frac{\partial f_j}{\partial p} = 0. \tag{B4}$$

Thus, we multiply the first equation in (2.15) multiplied by $3s$, integrate with respect to s on $\mathbb{R}^3$ and use (B1) to get the equations on $f = (f_1, f_2, f_3)$. Let us detail the calculations to derive the equation on f_1. First, multiplying (2.15) by $3s_1$ and integrating with respect to s leads to the following equation for f_1:

$$\frac{\partial f_1}{\partial t} + p \frac{\partial f_1}{\partial x} + \left(E_x - A_\perp \cdot \frac{\partial A_\perp}{\partial x} \right) \frac{\partial f_1}{\partial p}$$

$$- \beta \hbar \frac{\partial^2 A_z}{\partial x^2} \frac{\partial}{\partial p} \underbrace{\int (s_1 s_2 f + s_1 \partial_{s_2} f) \, ds}_{1} + \beta \hbar \frac{\partial^2 A_y}{\partial x^2} \frac{\partial}{\partial p} \underbrace{\int (s_1 s_3 f + s_1 \partial_{s_3} f) \, ds}_{2}$$

$$+ \frac{\partial A_z}{\partial x} \underbrace{\int 3 s_1 s_3 \frac{\partial f}{\partial s_1} \, ds}_{3} + \frac{\partial A_y}{\partial x} \underbrace{\int 3 s_1 s_2 \frac{\partial f}{\partial s_1} \, ds}_{4}$$

$$+ \frac{\partial A_y}{\partial x} \underbrace{\int -3 s_1^2 \frac{\partial f}{\partial s_2} \, ds}_{5} + \frac{\partial A_z}{\partial x} \underbrace{\int -3 s_1^2 \frac{\partial f}{\partial s_3} \, ds}_{6} = 0. \tag{B5}$$

Using the relations (B1) and (B2), we get that terms one and two are equal to zero, term three is equal to $-f_3/5$, term four is equal to $-f_2/5$, term five is equal to $-4f_2/5$, term six

is equal to $-4f_3/5$. Finally, we get the following equation for f_1:

$$\frac{\partial f_1}{\partial t} + p\frac{\partial f_1}{\partial x} + \left(E_x - \boldsymbol{A}_\perp \cdot \frac{\partial \boldsymbol{A}_\perp}{\partial x}\right)\frac{\partial f_1}{\partial p} - \frac{\partial A_z}{\partial x}f_3 - \frac{\partial A_y}{\partial x}f_2 = 0. \tag{B6}$$

Similar calculations lead to the equations for f_2 and f_3. Using the vector notation $\boldsymbol{f} = (f_1, f_2, f_3)$, the vector system satisfied by $\boldsymbol{f}$ can be reformulated as

$$\frac{\partial \boldsymbol{f}}{\partial t} + p\frac{\partial \boldsymbol{f}}{\partial x} + \left(E_x - \boldsymbol{A}_\perp \cdot \frac{\partial \boldsymbol{A}_\perp}{\partial x}\right)\frac{\partial \boldsymbol{f}}{\partial p} + \boldsymbol{B} \times \boldsymbol{f} + \beta\mathfrak{h}\frac{\partial \boldsymbol{B}}{\partial x}\frac{\partial f_0}{\partial p} = 0. \tag{B7}$$

It remains to be considered the coupling with the Maxwell equations, which involves integral with respect to $\boldsymbol{s}$ and p of the scalar unknown f. The Ampère equation simply becomes

$$\frac{\partial E_x}{\partial t} = -\int_{\mathbb{R}} pf_0 \, \mathrm{d}p, \tag{B8}$$

whereas the equations on E_y and E_z can be rewritten as function of $\boldsymbol{f}$, recalling that $f_j = 3\int_{\mathbb{S}^2} s_j f, \, \mathrm{d}\boldsymbol{s}$

$$\left.\begin{aligned} \frac{\partial E_y}{\partial t} &= -\frac{\partial^2 A_y}{\partial x^2} + A_y\int_{\mathbb{R}} f_0 \, \mathrm{d}p + \frac{\alpha\mathfrak{h}}{3}\int_{\mathbb{R}}\frac{\partial f_3}{\partial x}\mathrm{d}p, \\ \frac{\partial E_z}{\partial t} &= -\frac{\partial^2 A_z}{\partial x^2} + A_z\int_{\mathbb{R}} f_0 \, \mathrm{d}p - \frac{\alpha\mathfrak{h}}{3}\int_{\mathbb{R}}\frac{\partial f_2}{\partial x}\mathrm{d}p. \end{aligned}\right\} \tag{B9}$$

Appendix C. Solution of the subsystems involved in the Hamiltonian splitting

In this appendix, we detail the calculations of the solution of the five subsystems involved in the splitting, as described in § 2.3.

C.1. *Subsystem for $\mathcal{H}_p$*

The subsystem $\partial \mathcal{Z}/\partial t = \{\mathcal{Z}, \mathcal{H}_p\}$ associated with $\mathcal{H}_p = \frac{1}{2}\int p^2 f_0 \, \mathrm{d}x \, \mathrm{d}p$ is

$$\begin{cases} \dfrac{\partial f_0}{\partial t} = \{f_0, \mathcal{H}_p\} = -p\dfrac{\partial f_0}{\partial x}, \\[2mm] \dfrac{\partial \boldsymbol{f}}{\partial t} = \{\boldsymbol{f}, \mathcal{H}_p\} = -p\dfrac{\partial \boldsymbol{f}}{\partial x}, \\[2mm] \dfrac{\partial E_x}{\partial t} = \{E_x, \mathcal{H}_p\} = -\int_{\mathbb{R}} pf_0 \, \mathrm{d}p, \\[2mm] \dfrac{\partial \boldsymbol{E}_\perp}{\partial t} = \dfrac{\partial \boldsymbol{A}_\perp}{\partial t} = 0. \end{cases} \tag{C1}$$

We denote the initial datum as $(f_0^0(x, p), \boldsymbol{f}^0(x, p), E_x^0(x), \boldsymbol{E}_\perp^0(x), \boldsymbol{A}_\perp^0(x))$ at time $t = 0$. The solution at time t of this subsystem can be written explicitly as

$$\begin{cases} f_0(x, p, t) = f_0^0(x - pt, p), \quad \boldsymbol{f}(x, p, t) = \boldsymbol{f}^0(x - pt, p), \\[2mm] E_x(x, t) = E_x^0(x) - \displaystyle\int_0^t\int_{\mathbb{R}} pf_0(x, p, \tau) \, \mathrm{d}p \, \mathrm{d}\tau = E_x^0(x) - \int_0^t\int_{\mathbb{R}} pf_0^0(x - p\tau, p) \, \mathrm{d}p \, \mathrm{d}\tau, \\[2mm] \boldsymbol{E}_\perp(x, t) = \boldsymbol{E}_\perp^0(x), \quad \boldsymbol{A}_\perp(x, t) = \boldsymbol{A}_\perp^0(x). \end{cases} \tag{C2}$$

Next, we check that this solution correctly propagates the Poisson equation. To do so, we assume that the Poisson equation holds initially, i.e. $\partial E_x^0/\partial x = \int_{\mathbb{R}} f_0^0 \, dp - 1$. Then we have, by differentiating the expression of $E_x(t, x)$ with respect to x,

$$
\begin{aligned}
\frac{\partial E_x(x, t)}{\partial x} &= \frac{\partial E_x^0}{\partial x} - \int_0^t \int_{\mathbb{R}} p \frac{\partial f_0^0(x - p\tau, p)}{\partial x} \, dp \, d\tau = \frac{\partial E_x^0}{\partial x} + \int_0^t \int_{\mathbb{R}} \frac{\partial f_0^0(x - p\tau, p)}{\partial \tau} \, dp \, d\tau \\
&= \frac{\partial E_x^0}{\partial x} + \int_{\mathbb{R}} f_0^0(x - pt, p) \, dp - \int_{\mathbb{R}} f_0^0(x, p) \, dp = \int_{\mathbb{R}} f_0(x, p, t) \, dp - 1, \quad \text{(C3)}
\end{aligned}
$$

which proves that the Poisson equation is satisfied at time t.

C.2. Subsystem for $\mathcal{H}_A$

The subsystem $\partial \mathcal{Z}/\partial t = \{\mathcal{Z}, \mathcal{H}_A\}$ associated with the subhamiltonian $\mathcal{H}_A = \frac{1}{2} \int |A_\perp|^2 f_0 \, dx \, dp + \frac{1}{2} \int |\partial A_\perp/\partial x|^2 \, dx$ is

$$
\begin{cases}
\dfrac{\partial f_0}{\partial t} = \{f_0, \mathcal{H}_A\} = A_\perp \cdot \dfrac{\partial A_\perp}{\partial x} \dfrac{\partial f_0}{\partial p}, \\[2ex]
\dfrac{\partial f}{\partial t} = \{f, \mathcal{H}_A\} = A_\perp \cdot \dfrac{\partial A_\perp}{\partial x} \dfrac{\partial f}{\partial p}, \\[2ex]
\dfrac{\partial E_\perp}{\partial t} = \{E_\perp, \mathcal{H}_A\} = -\dfrac{\partial^2 A_\perp}{\partial x^2} + A_\perp \int_{\mathbb{R}} f_0 \, dp, \\[2ex]
\dfrac{\partial E_x}{\partial t} = \dfrac{\partial A_\perp}{\partial t} = 0.
\end{cases}
\quad \text{(C4)}
$$

We denote by $(f_0^0(x, p), f^0(x, p), E_x^0(x), E_\perp^0(x), A_\perp^0(x))$ the initial value at time $t = 0$. The exact solution at time t is

$$
\left.
\begin{aligned}
f_0(x, p, t) &= f_0^0 \left(x, p + t A_\perp^0(x) \cdot \frac{\partial A_\perp^0(x)}{\partial x} \right), \\[2ex]
f(x, p, t) &= f^0 \left(x, p + t A_\perp^0(x) \cdot \frac{\partial A_\perp^0(x)}{\partial x} \right), \\[2ex]
E_\perp(x, t) &= E_\perp^0(x) - t \frac{\partial^2 A_\perp^0(x)}{\partial x^2} + t A_\perp^0(x) \int_{\mathbb{R}} f_0^0(x, p) \, dp, \\[2ex]
E_x(x, t) &= E_x^0(x), \quad A_\perp(x, t) = A_\perp^0(x).
\end{aligned}
\right\}
\quad \text{(C5)}
$$

Let us remark that the third equation uses the fact that $\int_{\mathbb{R}} f_0(x, p, t) \, dp = \int_{\mathbb{R}} f_0^0(x, p) \, dp$, which can be obtained by integrating the first of (C4) with respect to p, i.e. $\partial_t (\int_{\mathbb{R}} f_0(x, p, t) \, dp) = 0$.

C.3. *Subsystem for* $\mathcal{H}_E$

The subsystem $\partial \mathcal{Z}/\partial t = \{\mathcal{Z}, \mathcal{H}_E\}$ associated with the subhamiltonian $\mathcal{H}_E = \frac{1}{2} \int |E|^2 \, dx$ is

$$
\begin{cases}
\dfrac{\partial f_0}{\partial t} = \{f_0, \mathcal{H}_E\} = -E_x \dfrac{\partial f_0}{\partial p}, \\[2mm]
\dfrac{\partial \boldsymbol{f}}{\partial t} = \{\boldsymbol{f}, \mathcal{H}_E\} = -E_x \dfrac{\partial \boldsymbol{f}}{\partial p}, \\[2mm]
\dfrac{\partial E_x}{\partial t} = \{E_x, \mathcal{H}_E\} = 0, \\[2mm]
\dfrac{\partial \boldsymbol{E}_\perp}{\partial t} = \{\boldsymbol{E}_\perp, \mathcal{H}_E\} = \boldsymbol{0}, \\[2mm]
\dfrac{\partial \boldsymbol{A}_\perp}{\partial t} = \{\boldsymbol{A}_\perp, \mathcal{H}_E\} = -\boldsymbol{E}_\perp.
\end{cases}
\tag{C6}
$$

With the initial value $(f_0^0(x, p), \boldsymbol{f}^0(x, p), E_x^0(x), \boldsymbol{E}_\perp^0(x), \boldsymbol{A}_\perp^0(x))$ at time $t = 0$, the solution at time t is as follows:

$$
\left.
\begin{aligned}
&f_0(x, p, t) = f_0^0(x, p - tE_x^0(x)), \quad \boldsymbol{f}(x, p, t) = \boldsymbol{f}^0(x, p - tE_x^0(x)), \\
&E_x(x, t) = E_x^0(x), \quad \boldsymbol{E}_\perp(x, t) = \boldsymbol{E}_\perp^0(x), \quad \boldsymbol{A}_\perp(x, t) = \boldsymbol{A}_\perp^0(x) - t\boldsymbol{E}_\perp^0(x).
\end{aligned}
\right\}
\tag{C7}
$$

C.4. *Subsystem for* $\mathcal{H}_2$

The subsystem $\partial \mathcal{Z}/\partial t = \{\mathcal{Z}, \mathcal{H}_2\}$ associated with the subhamiltonian $\mathcal{H}_2 = (\alpha \hbar/3) \int f_2 (\partial A_z/\partial x) \, dx \, dp$ is

$$
\begin{cases}
\dfrac{\partial f_0}{\partial t} = \{f_0, \mathcal{H}_2\} = \dfrac{\alpha \hbar}{3} \dfrac{\partial^2 A_z}{\partial x^2} \dfrac{\partial f_2}{\partial p}, \\[2mm]
\dfrac{\partial f_1}{\partial t} = \{f_1, \mathcal{H}_2\} = \dfrac{\partial A_z}{\partial x} f_3, \\[2mm]
\dfrac{\partial f_2}{\partial t} = \{f_2, \mathcal{H}_2\} = \beta \hbar \dfrac{\partial^2 A_z}{\partial x^2} \dfrac{\partial f_0}{\partial p}, \\[2mm]
\dfrac{\partial f_3}{\partial t} = \{f_3, \mathcal{H}_2\} = -\dfrac{\partial A_z}{\partial x} f_1, \\[2mm]
\dfrac{\partial E_z}{\partial t} = \{E_z, \mathcal{H}_2\} = -\dfrac{\alpha \hbar}{3} \int_{\mathbb{R}} \dfrac{\partial f_2}{\partial x} \, dp, \\[2mm]
\dfrac{\partial E_x}{\partial t} = \dfrac{\partial E_y}{\partial t} = \dfrac{\partial A_\perp}{\partial t} = 0.
\end{cases}
\tag{C8}
$$

In this subsystem, we observe some coupling between the distribution functions. To write down the exact solution, we reformulate the equations for $(f_0, \boldsymbol{f})$, using $A_z(x, t) = A_z^0(x)$, as follows:

$$
\left.
\begin{aligned}
&\partial_t \begin{pmatrix} f_1 \\ f_3 \end{pmatrix} - \dfrac{\partial A_z^0}{\partial x} J \begin{pmatrix} f_1 \\ f_3 \end{pmatrix} = 0, \\[3mm]
&\partial_t \begin{pmatrix} f_0 \\ f_2 \end{pmatrix} - \hbar \dfrac{\partial^2 A_z^0}{\partial x^2} \begin{pmatrix} 0 & \dfrac{\alpha}{3} \\ \beta & 0 \end{pmatrix} \partial_p \begin{pmatrix} f_0 \\ f_2 \end{pmatrix} = 0,
\end{aligned}
\right\}
\tag{C9}
$$

where J denotes the symplectic matrix

$$J = \begin{pmatrix} 0 & 1 \\ -1 & 0 \end{pmatrix}. \tag{C10}$$

With the initial data $(f_0^0(x, p), \boldsymbol{f}^0(x, p), E_x^0(x), \boldsymbol{E}_\perp^0(x), \boldsymbol{A}_\perp^0(x))$ at time $t = 0$, the exact solution for the first system is

$$\begin{pmatrix} f_1 \\ f_3 \end{pmatrix}(x, p, t) = \exp\left(\frac{\partial A_z^0(x)}{\partial x} Jt\right) \begin{pmatrix} f_1^0(x, p) \\ f_3^0(x, p) \end{pmatrix}, \quad \text{with } \exp(Js) = \begin{pmatrix} \cos(s) & \sin(s) \\ -\sin(s) & \cos(s) \end{pmatrix}. \tag{C11}$$

Let us now focus on the second system

$$\partial_t \begin{pmatrix} f_0 \\ f_2 \end{pmatrix} - \hbar \frac{\partial^2 A_z^0}{\partial x^2} \begin{pmatrix} 0 & \frac{\alpha}{3} \\ \beta & 0 \end{pmatrix} \partial_p \begin{pmatrix} f_0 \\ f_2 \end{pmatrix} = 0. \tag{C12}$$

By the eigen-decomposition (to simplify, we assume $\alpha > 0$, $\beta > 0$ here)

$$\begin{pmatrix} -\frac{1}{2}\sqrt{\frac{3\beta}{\alpha}} & \frac{1}{2} \\ \frac{1}{2}\sqrt{\frac{3\beta}{\alpha}} & \frac{1}{2} \end{pmatrix} \begin{pmatrix} 0 & \frac{\alpha}{3} \\ \beta & 0 \end{pmatrix} \begin{pmatrix} -\sqrt{\frac{\alpha}{3\beta}} & \sqrt{\frac{\alpha}{3\beta}} \\ 1 & 1 \end{pmatrix} = \begin{pmatrix} -\sqrt{\frac{\alpha\beta}{3}} & 0 \\ 0 & \sqrt{\frac{\alpha\beta}{3}} \end{pmatrix}, \tag{C13}$$

then, one can diagonalize the transport equation to get

$$\partial_t \begin{pmatrix} -\frac{1}{2}\sqrt{\frac{3\beta}{\alpha}} f_0 + \frac{1}{2} f_2 \\ \frac{1}{2}\sqrt{\frac{3\beta}{\alpha}} f_0 + \frac{1}{2} f_2 \end{pmatrix} - \hbar \frac{\partial^2 A_z^0}{\partial x^2} \begin{pmatrix} -\sqrt{\frac{\alpha\beta}{3}} & 0 \\ 0 & \sqrt{\frac{\alpha\beta}{3}} \end{pmatrix} \partial_p \begin{pmatrix} -\frac{1}{2}\sqrt{\frac{3\beta}{\alpha}} f_0 + \frac{1}{2} f_2 \\ \frac{1}{2}\sqrt{\frac{3\beta}{\alpha}} f_0 + \frac{1}{2} f_2 \end{pmatrix} = 0. \tag{C14}$$

Finally, we can solve the transport equation

$$\left(\mp \frac{1}{2}\sqrt{\frac{3\beta}{\alpha}} f_0 + \frac{1}{2} f_2\right)(x, p, t) = \left(\mp \frac{1}{2}\sqrt{\frac{3\beta}{\alpha}} f_0^0 + \frac{1}{2} f_2^0\right)\left(x, p \mp t\sqrt{\frac{\alpha\beta}{3}}\hbar \frac{\partial^2 A_z^0}{\partial x^2}(x)\right), \tag{C15}$$

and compute the exact solution at time t as follows:

$$
\left.
\begin{aligned}
f_1(x, p, t) &= \cos\left(t\frac{\partial A_z^0(x)}{\partial x}\right) f_1^0(x, p) + \sin\left(t\frac{\partial A_z^0(x)}{\partial x}\right) f_3^0(x, p), \\
f_3(x, p, t) &= -\sin\left(t\frac{\partial A_z^0(x)}{\partial x}\right) f_1^0(x, p) + \cos\left(t\frac{\partial A_z^0(x)}{\partial x}\right) f_3^0(x, p) \\
f_0(x, p, t) &= -\sqrt{\frac{\alpha}{3\beta}}\left(-\frac{1}{2}\sqrt{\frac{3\beta}{\alpha}}f_0^0 + \frac{1}{2}f_2^0\right)\left(x, p - t\sqrt{\frac{\alpha\beta}{3}}\hbar\frac{\partial^2 A_z^0}{\partial x^2}(x)\right) \\
&\quad + \sqrt{\frac{\alpha}{3\beta}}\left(\frac{1}{2}\sqrt{\frac{3\beta}{\alpha}}f_0^0 + \frac{1}{2}f_2^0\right)\left(x, p + t\sqrt{\frac{\alpha\beta}{3}}\hbar\frac{\partial^2 A_z^0}{\partial x^2}(x)\right), \\
f_2(x, p, t) &= \left(-\frac{1}{2}\sqrt{\frac{3\beta}{\alpha}}f_0^0 + \frac{1}{2}f_2^0\right)\left(x, p - t\sqrt{\frac{\alpha\beta}{3}}\hbar\frac{\partial^2 A_z^0}{\partial x^2}(x)\right) \\
&\quad + \left(\frac{1}{2}\sqrt{\frac{3\beta}{\alpha}}f_0^0 + \frac{1}{2}f_2^0\right)\left(x, p + t\sqrt{\frac{\alpha\beta}{3}}\hbar\frac{\partial^2 A_z^0}{\partial x^2}(x)\right), \\
E_z(x, t) &= E_z^0(x) - t\frac{\alpha\hbar}{3}\int_{\mathbb{R}}\frac{\partial f_2^0}{\partial x}\,\mathrm{d}p.
\end{aligned}
\right\} \quad \text{(C16)}
$$

The last equation can easily obtained by verifying that $\int_{\mathbb{R}} f_2(x, p, t)\,\mathrm{d}p = \int_{\mathbb{R}} f_2^0(x, p, t)\,\mathrm{d}p$.

C.5. *Subsystem for $\mathcal{H}_3$*

The subsystem $\partial \mathcal{Z}/\partial t = \{\mathcal{Z}, \mathcal{H}_3\}$ associated with the subhamiltonian $\mathcal{H}_3 = -\int_\Omega (\alpha\hbar/3)\, f_3(\partial A_y/\partial x)\,\mathrm{d}x\,\mathrm{d}p$ is

$$
\left\{
\begin{aligned}
\frac{\partial f_0}{\partial t} &= \{f_0, \mathcal{H}_3\} = -\frac{\alpha\hbar}{3}\frac{\partial^2 A_y}{\partial x^2}\frac{\partial f_3}{\partial p}, \\
\frac{\partial f_1}{\partial t} &= \{f_1, \mathcal{H}_3\} = \frac{\partial A_y}{\partial x}f_2, \\
\frac{\partial f_2}{\partial t} &= \{f_2, \mathcal{H}_3\} = -\frac{\partial A_y}{\partial x}f_1, \\
\frac{\partial f_3}{\partial t} &= -\{f_3, \mathcal{H}_3\} = -\beta\hbar\frac{\partial^2 A_y}{\partial x^2}\frac{\partial f_0}{\partial p}, \\
\frac{\partial E_y}{\partial t} &= \{E_y, \mathcal{H}_3\} = \frac{\alpha\hbar}{3}\int_{\mathbb{R}}\frac{\partial f_3}{\partial x}\,\mathrm{d}p, \\
\frac{\partial E_x}{\partial t} &= \frac{\partial E_z}{\partial t} = \frac{\partial A_\perp}{\partial t} = 0.
\end{aligned}
\right. \quad \text{(C17)}
$$

This subsystem is very similar to the $\mathcal{H}_2$ one, hence, as previously, we reformulate the equations on the distribution functions as

$$
\left.\begin{aligned}
\partial_t \begin{pmatrix} f_1 \\ f_2 \end{pmatrix} - \frac{\partial A_y^0}{\partial x} J \begin{pmatrix} f_1 \\ f_2 \end{pmatrix} &= 0, \\
\partial_t \begin{pmatrix} f_0 \\ f_3 \end{pmatrix} + \hbar \frac{\partial^2 A_y^0}{\partial x^2} \begin{pmatrix} 0 & \frac{\alpha}{3} \\ \beta & 0 \end{pmatrix} \partial_p \begin{pmatrix} f_0 \\ f_3 \end{pmatrix} &= 0,
\end{aligned}\right\}
\tag{C18}
$$

with initial data $(f_0^0(x, p), \boldsymbol{f}^0(x, p), E_x^0(x), \boldsymbol{E}_\perp^0(x), \boldsymbol{A}_\perp^0(x))$ at time $t = 0$. We derive similar formulae with $\mathcal{H}_2$ for the exact solution at time t

$$
\left.\begin{aligned}
f_1(x, p, t) &= \cos\left(t \frac{\partial A_y^0(x)}{\partial x}\right) f_1^0(x, p) + \sin\left(t \frac{\partial A_y^0(x)}{\partial x}\right) f_2^0(x, p), \\
f_2(x, p, t) &= -\sin\left(t \frac{\partial A_y^0(x)}{\partial x}\right) f_1^0(x, p) + \cos\left(t \frac{\partial A_y^0(x)}{\partial x}\right) f_2^0(x, p), \\
f_0(x, p, t) &= -\sqrt{\frac{\alpha}{3\beta}} \left(-\frac{1}{2}\sqrt{\frac{3\beta}{\alpha}} f_0^0 + \frac{1}{2} f_3^0\right) \left(x, p + t\sqrt{\frac{\alpha\beta}{3}} \hbar \frac{\partial^2 A_y^0}{\partial x^2}(x)\right) \\
&\quad + \sqrt{\frac{\alpha}{3\beta}} \left(\frac{1}{2}\sqrt{\frac{3\beta}{\alpha}} f_0^0 + \frac{1}{2} f_3^0\right) \left(x, p - t\sqrt{\frac{\alpha\beta}{3}} \hbar \frac{\partial^2 A_y^0}{\partial x^2}(x)\right), \\
f_3(x, p, t) &= \left(-\frac{1}{2}\sqrt{\frac{3\beta}{\alpha}} f_0^0 + \frac{1}{2} f_3^0\right) \left(x, p + t\sqrt{\frac{\alpha\beta}{3}} \hbar \frac{\partial^2 A_y^0}{\partial x^2}(x)\right) \\
&\quad + \left(\frac{1}{2}\sqrt{\frac{3\beta}{\alpha}} f_0^0 + \frac{1}{2} f_3^0\right) \left(x, p - t\sqrt{\frac{\alpha\beta}{3}} \hbar \frac{\partial^2 A_y^0}{\partial x^2}(x)\right), \\
E_y(x, t) &= E_y^0(x) + t \frac{\alpha\hbar}{3} \int_{\mathbb{R}} \frac{\partial f_3^0}{\partial x} \mathrm{d}p, \\
\boldsymbol{A}_\perp(x, t) &= \boldsymbol{A}_\perp^0(x), \quad E_x(x, t) = E_x^0(x), \quad E_z(x, t) = E_z^0(x).
\end{aligned}\right\}
\tag{C19}
$$

To compute the solution $E_y(x, t)$, we use the fact that $\int_{\mathbb{R}} f_3(x, p, t) \, \mathrm{d}p = \int_{\mathbb{R}} f_3^0(x, p) \mathrm{d}p$.

C.6. *Fully discrete numerical scheme*

Finally, we consider the phase space and time discretization to get the full discretization for above vectorial model.

We assume that the computational domain is $[0, L] \times [-p_{\max}, p_{\max}]$ for x and p. The system is periodic in the x direction with period L and has compact support on $[-p_{\max}, p_{\max}]$ in p direction. The mesh is as follows:

$$
x_j = (j - 1)\Delta x, \quad j = 1, \ldots, N_x, \quad \Delta x = L/N_x, \quad (N_x \text{ is odd})
\tag{C20}
$$

$$
p_{\ell-1} = (\ell - 1)\Delta p - p_{\max}, \quad \ell = 1, \ldots, N_p, \quad \Delta p = 2p_{\max}/N_p.
\tag{C21}
$$

C.6.1. *Phase space representation*

Here we use the same discretization method as in Li *et al.* (2020). We first present the spatial discretization of E_x in detail, the same strategy can be used to $E_\perp$ and $A_\perp$. Denoting $E_{x,j} = E_x(x_j, t)$, we use the spectral Fourier expansion to approximate E_x as it is periodic in the x direction,

$$E_{x,j} = \sum_{k=-(N_x-1)/2}^{(N_x-1)/2} \hat{E}_{x,k}(t) \exp(2\pi ijk/N_x), \quad \text{for } j = 1, \dots, N_x. \tag{C22}$$

For the distribution functions (f_0, f), we use a spectral Fourier expansion for the x direction and a finite-volume method for the p direction. For simplicity, we only show the representation for f_0, the notations for f being the same. Here $f_{0,j,\ell}(t)$ denotes the average of $f_0(x_j, p, t)$ over a cell $C_\ell = [p_{\ell-1/2}, p_{l+1/2}]$ with the midpoint $p_{\ell-1/2} = (\ell - 1/2)\Delta p - P_L$, that is

$$f_{0,j,\ell}(t) = \frac{1}{\Delta p} \int_{C_\ell} f_0(x_j, p, t) \, dp, \tag{C23}$$

and also by Fourier expansion in x direction, then

$$f_{0,j,\ell}(t) = \sum_{k=-(N_x-1)/2}^{(N_x-1)/2} \hat{f}_{0,k,\ell}(t) \exp(2\pi ijk/N_x), \quad j = 1, \dots, N_x. \tag{C24}$$

To evaluate the value of f_0 off-grid in p direction, we need to reconstruct a continuous function by using the cell average quantity $f_{0,j,\ell}$. We refer to Crouseilles, Mehrenberger & Sonnendrücker (2010) and Zerroukat, Wood & Staniforth (2006) for a presentation of the parabolic spline method to construct a second-order polynomial approximation. To present the main idea, we consider a linear advection problem in the p direction

$$\frac{\partial f}{\partial t} + a\frac{\partial f}{\partial x} = 0. \tag{C25}$$

From the conservation of the volume, we have the following identity:

$$f_{j,\ell}(t) = \frac{1}{\Delta p} \int_{p_{\ell-1/2}}^{p_{\ell+1/2}} f(x_j, p, t) \, dp = \frac{1}{\Delta p} \int_{p_{\ell-1/2}-at}^{p_{\ell+1/2}-at} f(x_j, p, 0) \, dp. \tag{C26}$$

For simplicity, we denote $q \in [1, N_p]$ the index such that $p_{\ell+1/2} - at \in [p_{q-1/2}, p_{q+1/2}]$ i.e. $p_{\ell+1/2} - at \in C_q$, then we have

$$f_{j,\ell}(t) = \frac{1}{\Delta p} \int_{p_{q-1/2}-at}^{p_{q-1/2}} f(x_j, p, 0) \, dp + f_{j,q}(0) - \frac{1}{\Delta p} \int_{p_{q+1/2}}^{p_{q+1/2}-at} f(x_j, p, 0) \, dp. \tag{C27}$$

Here, we need to reconstruct a polynomial function $f(x_j, p, 0)$ using the averages $f_{j,l}(0)$ with the parabolic spline method approach. The full discretization of the different subsystems uses the tools described in Li *et al.* (2020).

REFERENCES

BEAUREPAIRE, E., MERLE, J.-C., DAUNOIS, A. & BIGOT, J.-Y. 1996 Ultrafast spin dynamics in ferromagnetic nickel. *Phys. Rev. Lett.* **76** (22), 4250.

BIGOT, J.-Y. & VOMIR, M. 2013 Ultrafast magnetization dynamics of nanostructures. *Ann. Phys.* **525** (1–2), 2–30.

BIGOT, J.-Y., VOMIR, M. & BEAUREPAIRE, E. 2009 Coherent ultrafast magnetism induced by femtosecond laser pulses. *Nat. Phys.* **5** (7), 515–520.

BRODIN, G., HOLKUNDKAR, A. & MARKLUND, M. 2013 Particle-in-cell simulations of electron spin effects in plasmas. *J. Plasma Phys.* **79** (4), 377–382.

BRODIN, G., MARKLUND, M., ZAMANIAN, J., ERICSSON, Å. & MANA, P.L. 2008 Effects of the g factor in semiclassical kinetic plasma theory. *Phys. Rev. Lett.* **101** (24), 245002.

BRODIN, G., MARKLUND, M., ZAMANIAN, J. & STEFAN, M. 2011 Spin and magnetization effects in plasmas. *Plasma Phys. Control. Fusion* **53** (7), 074013.

CHOI, G.-M., MIN, B.-C., LEE, K.-J. & CAHILL, D.G. 2014 Spin current generated by thermally driven ultrafast demagnetization. *Nat. Commun.* **5** (1), 1–8.

CRESTETTO, A., CROUSEILLES, N., LI, Y. & MASSOT, J. 2022 Comparison of high-order Eulerian methods for electron hybrid model. *J. Comput. Phys.* **451**, 110857.

CROUSEILLES, N., EINKEMMER, L. & FAOU, E. 2015 Hamiltonian splitting for the Vlasov–Maxwell equations. *J. Comput. Phys.* **283**, 224–240.

CROUSEILLES, N., HERVIEUX, P.-A., LI, Y., MANFREDI, G. & SUN, Y. 2021 Geometric particle-in-cell methods for the Vlasov–Maxwell equations with spin effects. *J. Plasma Phys.* **87** (3).

CROUSEILLES, N., MEHRENBERGER, M. & SONNENDRÜCKER, E. 2010 Conservative semi-lagrangian schemes for Vlasov equations. *J. Comput. Phys.* **229** (6), 1927–1953.

DAUGER, D., DECYK, V. & DAWSON, J. 2005 Using semiclassical trajectories for the time-evolution of interacting quantum-mechanical systems. *J. Comput. Phys.* **209** (2), 559–581.

FORSLUND, D., KINDEL, J. & LINDMAN, E. 1975 Theory of stimulated scattering processes in laser-irradiated plasmas. *Phys. Fluids* **18**, 1002.

GHIZZO, A., BERTRAND, P., SHOUCRI, M., JOHNSTON, T., FUALKOW, E. & FEIX, M. 1990 A Vlasov code for the numerical simulation of stimulated Raman scattering. *J. Comput. Phys.* **90** (2), 431–457.

HINSCHBERGER, Y. & HERVIEUX, P.-A. 2012 Foldy-Wouthuysen transformation applied to the interaction of an electron with ultrafast electromagnetic fields. *Phys. Lett.* A **376** (6), 813–819.

HUOT, F., GHIZZO, A., BERTRAND, P., SONNENDRÜCKER, E. & COULAUD, O. 2003 Instability of the time splitting scheme for the one-dimensional and relativistic Vlasov–Maxwell system. *J. Comput. Phys.* **185** (2), 512–531.

HURST, J., HERVIEUX, P.-A. & MANFREDI, G. 2018 Spin current generation by ultrafast laser pulses in ferromagnetic nickel films. *Phys. Rev.* B **97**, 014424.

HURST, J., MORANDI, O., MANFREDI, G. & HERVIEUX, P.-A. 2014 Semiclassical Vlasov and fluid models for an electron gas with spin effects. *Eur. Phys. J.* D **68** (6), 1–11.

HURST, J., MORANDI, O., MANFREDI, G. & HERVIEUX, P.-A. 2017 Phase-space methods for the spin dynamics in condensed matter systems. *Phil. Trans. R. Soc. Lond.* A **375** (20160199).

KRAUS, M., KORMANN, K., MORRISON, P.J. & SONNENDRÜCKER, E. 2017 Gempic: geometric electromagnetic particle-in-cell methods. *J. Plasma Phys.* **83** (4).

KRIEGER, K., DEWHURST, J., ELLIOTT, P., SHARMA, S. & GROSS, E. 2015 Laser-induced demagnetization at ultrashort time scales: predictions of TDDFT. *J. Chem. Theory Comput.* **11** (10), 4870–4874.

KRIEGER, K., ELLIOTT, P., MÜLLER, T., SINGH, N., DEWHURST, J., GROSS, E. & SHARMA, S. 2017 Ultrafast demagnetization in bulk versus thin films: an ab initio study. *J. Phys.: Condens. Matter* **29** (22), 224001.

LI, F., DECYK, V.K., MILLER, K.G., TABLEMAN, A., TSUNG, F.S., VRANIC, M., FONSECA, R.A. & MORI, W.B. 2021 Accurately simulating nine-dimensional phase space of relativistic particles in strong fields. *J. Comput. Phys.* **438**, 110367.

LI, Y., SUN, Y. & CROUSEILLES, N. 2020 Numerical simulations of one laser-plasma model based on Poisson structure. *J. Comput. Phys.* **405**, 109172.

MANFREDI, G., HERVIEUX, P.-A. & CROUSEILLES, N. 2022 Spin effects in ultrafast laser-plasma interactions. *Eur. Phys. J. Spec. Top.* 1–7. https://doi.org/10.1140/epjs/s11734-022-00669-5.

MANFREDI, G., HERVIEUX, P.-A. & HURST, J. 2019 Phase-space modeling of solid-state plasmas. *Rev. Mod. Plasma Phys.* **3** (1), 1–55.

MARKLUND, M. & MORRISON, P. 2011 Gauge-free hamiltonian structure of the spin Maxwell–Vlasov equations. *Phys. Lett.* A **375** (24), 2362–2365.

MARKLUND, M., ZAMANIAN, J. & BRODIN, G. 2010 Spin kinetic theory–quantum kinetic theory in extended phase space. *Transp. Theory Stat. Phys.* **39** (5–7), 502–523.

MOLDABEKOV, Z.A., BONITZ, M. & RAMAZANOV, T. 2018 Theoretical foundations of quantum hydrodynamics for plasmas. *Phys. Plasmas* **25** (3), 031903.

QIN, H., LIU, J., XIAO, J., ZHANG, R., HE, Y., WANG, Y., SUN, Y., BURBY, J., ELLISON, L. & ZHOU, Y. 2015 Canonical symplectic Particle-In-Cell method for long-term large-scale simulations of the Vlasov-Maxwell equations. *Nucl. Fusion* **56** (1), 014001.

SCHELLEKENS, A., KUIPER, K., DE WIT, R. & KOOPMANS, B. 2014 Ultrafast spin-transfer torque driven by femtosecond pulsed-laser excitation. *Nat. Commun.* **5** (1), 1–7.

TONGE, J., DAUGER, D.E. & DECYK, V.K. 2004 Two-dimensional semiclassical particle-in-cell code for simulation of quantum plasmas. *Comput. Phys. Commun.* **164** (1–3), 279–285.

XIAO, J., QIN, H., LIU, J., HE, Y., ZHANG, R. & SUN, Y. 2015 Explicit high-order non-canonical symplectic Particle-In-Cell algorithms for Vlasov-Maxwell systems. *Phys. Plasmas* **22** (11), 112504.

ZAMANIAN, J., MARKLUND, M. & BRODIN, G. 2010 Scalar quantum kinetic theory for spin-1/2 particles: mean field theory. *New J. Phys.* **12** (4), 043019.

ZERROUKAT, M., WOOD, N. & STANIFORTH, A. 2006 The parabolic spline method for conservative transport problems. *Intl J. Numer. Meth. Fluids* **51** (11), 1297–1318.